POLITECNICO DI MILANO

Faculty of Industrial and Information Engineering

Laurea Magistrale (MSc) in Engineering Physics

On – chip photon – pair sources by direct laser writing with a femtosecond laser

Supervisor: **Dr. Roberto Osellame**
Co-supervisor: **Dr. Giacomo Corrielli**

Thesis of:
Simone Atzeni
Student ID: 819846

Academic Year 2015/16

Abstract

Photon number state generation is a thriving field of research, since progress in this area will directly affect the development of a wide set of applications. Several methods are being sifted to increase the capabilities of single photon sources and the integrated optics approach represents a promising strategy. This thesis deals with the development of integrated optical components for the generation of photon-pairs at telecom wavelength through spontaneous parametric down conversion in nonlinear waveguides. Exploiting femtosecond laser micromachining technique, a pair of waveguides in a nonlinear poled crystal was fabricated. A classical characterization was performed through second harmonic generation process and an overlap between the two SHG curves above 99 % was retrieved, showing comparable nonlinear properties between waveguides. To route and manipulate photons, balanced directional couplers at the fundamental and down-converted wavelength were realized in glass. A thermal phase adjuster was machined on the gold sputtered surface of the first directional coupler to control the overall phase and the output state of the source.

Sommario

La generazione e la manipolazione di stati a singolo fotone rappresentano sia un pilastro sia il collo di bottiglia nello sviluppo della tecnologia quantistica. La produzione on-demand di singoli fotoni è l'elemento cruciale in una serie di applicazioni innovative: la generazione di chiavi crittografiche, la possibilità di aumentare esponenzialmente la potenza di calcolo e di superare il Limite Quantistico Standard. La piena maturazione delle potenzialità delle sorgenti a singolo fotone è tuttavia ben lontana dall'essere raggiunta a causa di notevoli limitazioni tecnologiche nella loro fabbricazione.

In questo contesto, il passaggio da componenti ottici bulk ad integrati rappresenta una delle strategie più promettenti per il superamento dello stato dell'arte nella generazione di singoli fotoni. Attraverso l'integrazione su chip è possibile realizzare circuiti ottici complessi con una riduzione delle dimensioni del singolo componente e con un aumento della stabilità del dispositivo complessivo. Nonostante la realizzazione di circuiti lineari integrati abbia fatto passi da gigante, lo sviluppo di sorgenti di luce quantistica su chip è ancora in fase embrionale.

In questo lavoro di tesi ci siamo occupati dello sviluppo dei componenti ottici integrati per la produzione di una sorgente di coppie di fotoni basata sul processo di spontaneous parametric down conversion alle lunghezze d'onda telecom. Per la fabbricazione dei componenti ottici abbiamo utilizzato la tecnica della microfabbricazione con laser a femtosecondi. Tramite questa tecnica, guide d'onda e circuiti ottici possono essere realizzati in una vasta serie di substrati regolando i parametri di processo e senza dover ricorrere a maschere fotolitografiche. La pro-

totipazione di circuiti ottici tridimensionali ad alta qualità avviene in maniera diretta ed economica, rendendo questa tecnologia ideale per lo sviluppo di dispositivi innovativi nel campo delle tecnologie quantistiche.

Contents

List of figures

List of Tables

Introduction

The generation and the manipulation of single-photon state represent both a cornerstone and a bottleneck for the development of quantum photonics. The on-demand production of single-photons opens the doors to a set of innovative applications: the production of a secure cryptographic key in the area of quantum communication, the possibility to overcome classical computing and to go beyond the standard quantum limit. However, considerable advancement still has to be accomplished to fully exploit the capabilities of single photon sources.

An effective approach to upgrade current state-of-the-art in single photon generation can be represented by integrated quantum photonics. Integrated optics technologies permit the realization of scalable quantum circuits being advantageous in terms of stability, complexity and footprint with respect to the bulk approach. In this framework, the realization of integrated linear circuits have made great strides, while the development of sources of quantum light on chip is still in the embryonic phase. Due to high brightness and intrinsic stability, spontaneous parametric down conversion (PDC) in periodically poled non-linear waveguides represents a promising approach to make progress in the field of integrated quantum source.

The aim of this thesis is the development of the integrated optics components of a photon-pair source at telecom wavelength, based on spontaneous parametric down conversion in nonlinear waveguides. To attain our purpose, we employ the femtosecond laser micromachining technique. This fabrication method allows to inscribe optical waveguides in several transparent substrates just tailoring the pro-

cessing parameters and with no need of dedicated photolithographic masks. In particular, it allows the prototyping of high quality three dimensional optical circuits in a direct and cost effective manner proving as an ideal technology to develop innovative quantum design.

The thesis is organized as follows: Chapter 1 introduces basic concepts on quantum state and single photon sources. Chapter 2 deals with the basic principles of femtosecond laser micromachining technique in amorphous and crystalline media. Chapter 3 is dedicated to the description of the experimental setup and the characterization method. Chapter 4 describes the idea regarding our photon source and its elementary components. The fabrication and the characterization of the integrated devices are discussed in Chapter 5 and 6.

1
Single-Photon Sources

In this chapter a brief introduction to single-photon sources is presented. In section 1.1 a general description of Fock states and their properties is provided. In section 1.2 the ideal single-photon source, its typical practical configurations and applications are described.

1.1 FOCK STATES

A number state or a Fock state is a quantum state in which the number of particles n is a precisely fixed integer. In quantum optics the grainy nature of light appears and photons reveal themself. What is a photon? A photon is defined as an elementary excitation of a single mode of the quantized electromagnetic field. The quantization of the electromagnetic energy was first proposed by Planck in 1900 [1] to explain the thermodynamics of the black-body radiation. In 1905 Einstein [2] exploited this concept to explain the photoelectric effect. Actually, the photoelectric effect can be fully interpreted in the semi-classical approach, where matter is quantized and light behaves as a classical wave. The term "photon" was first coined by G.N. Lewis in 1926 [3]. In 1927 Dirac introduced the first formal quantization of the electromagnetic field. After the introduction of the correlation experiment by Hambury-Brown and Twiss in 1956 [4], a deep analysis of the quantum properties of light and in particular of the second order coherence started. Number-states were finally described as a special case of squeezed light [5].

1.1.1 PROPERTIES OF SINGLE-PHOTON STATES

In order to understand the optical properties and the advantages of single-photon sources with respect to standard light source, a brief review of quantum optics basic notions is presented.

ELECTROMAGNETIC FIELD QUANTIZATION

A mode of the electromagnetic field in a cavity with volume L^3 can be quantized as an harmonic oscillator. Operators $a^{\dagger}_{\vec{k},\vec{\varepsilon}}$ and $a_{\vec{k},\vec{\varepsilon}}$ respectively, create and annihilate a photon with wave vector $\vec{k}$, angular frequency w_k and polarization $\vec{\varepsilon}$. In the Heisenberg picture, the electric field operator can be decomposed in two Hermitian-conjugate terms:

$$\vec{E}(\vec{r},t) = \vec{E}^{(-)}(\vec{r},t) + \vec{E}^{(+)}(\vec{r},t), \tag{1.1}$$

where

$$\vec{E}^{(-)}(\vec{r},t) = i \sum_{\vec{k},\vec{\varepsilon}} \sqrt{\frac{\hbar w_k}{2\varepsilon_0 L^3}} \vec{\varepsilon} \, a^\dagger_{\vec{k},\vec{\varepsilon}} \, e^{i(\vec{k}\cdot\vec{r} - w_k t)} \tag{1.2}$$

After the definition of the magnetic field operator with an analogue procedure, the quantized electromagnetic field can be described by the Hamiltonian operator in the following formula:

$$H_R = \frac{1}{2} \sum_{\vec{k},\vec{\varepsilon}} \hbar w_k \left(a^\dagger_{\vec{k},\vec{\varepsilon}} a_{\vec{k},\vec{\varepsilon}} + a_{\vec{k},\vec{\varepsilon}} a^\dagger_{\vec{k},\vec{\varepsilon}} \right) \tag{1.3}$$

The average number of photons in a given mode is described by the photon number operator $\hat{n} = a^\dagger a$. The eigenstates of this operator are called Fock states and are defined by:

$$a^\dagger a \ket{n} = n \ket{n}, \tag{1.4}$$

where n is the number of photons in the number state $\ket{n}$. The annihilation and the creation operation can be applied to $\ket{n}$ according to:

$$a \ket{n} = \sqrt{n} \ket{n-1} \tag{1.5a}$$
$$a^\dagger \ket{n} = \sqrt{n+1} \ket{n+1} \tag{1.5b}$$
$$a \ket{0} = 0 \tag{1.5c}$$

STATISTICAL PROPERTIES OF LIGHT

Neglecting spatial coherence aspects, the characterization of the statistical properties of light into a given state can be defined by the following three functions of time:

- ISTANTANEOUS INTENSITY:

$$I(t) = 2\varepsilon_0 c \langle E^{(-)}(t) E^{(+)}(t) \rangle \tag{1.6}$$
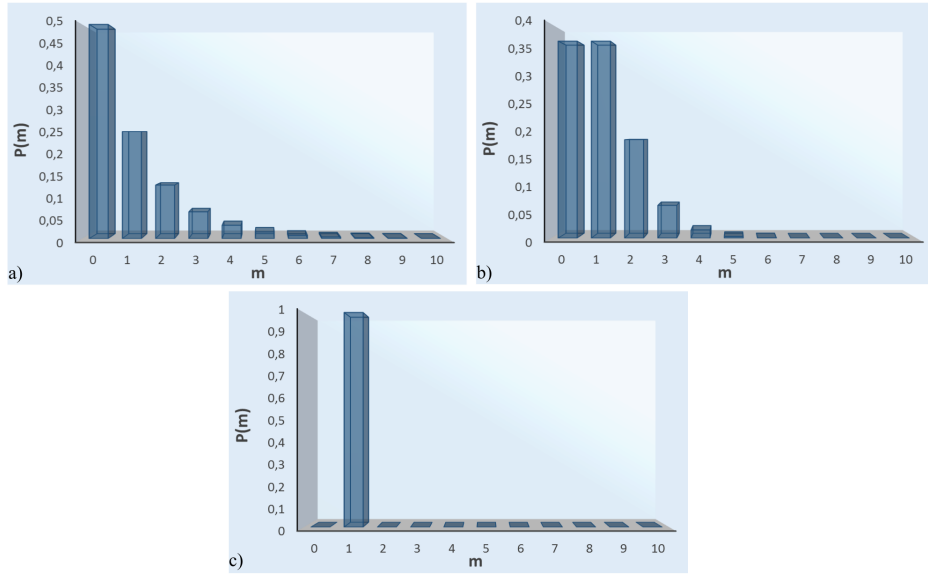
Figure 1.1.1: Photon number distribution for three sources with an average photon number $\langle n \rangle = 1$: (a) Thermal source, (b) Coherent light source and (c) Single-photon state.

- FIRST ORDER CORRELATION FUNCTION :

$$g^{(1)}(\tau) = \frac{\langle E^{(-)}(t+\tau)E^{(+)}(t)\rangle}{\langle E^{(-)}(t)E^{(+)}(t)\rangle}, \tag{1.7}$$

which is insensitive to photon statistics and is proportional to the average number of photons and the coherence length of the source.

- SECOND ORDER CORRELATION FUNCTION [6] :

$$g^{(2)}(\tau) = \frac{\langle E^{(-)}(t)E^{(-)}(t+\tau)E^{(+)}(t+\tau)E^{(+)}(t)\rangle}{\langle E^{(-)}(t)E^{(+)}(t)\rangle^2} \tag{1.8}$$

Depending on the value of $g^{(2)}(0)$, different light sources can be classified as super-Poissonian, Poissonian and sub-Poissonian. An example for each class follows:

6

1. Thermal light: The field of a conventional macroscopic source as a lamp can be represented by the superposition of many incoherent waves, each produced by an independent emitter with a random phase and delay.

$$\vec{E} = \sum_i e^{i\varphi_i}\vec{E}_o(t - t_i) \tag{1.9}$$

Assuming the same time-dependence for each emitter, the total field correlation function is identical to that of an individual emitter and its Fourier-transform corresponds to the spectrum of the macroscopic source. Averaging over all the phases, the following relations can be retrieved:

$$g^{(2)}(\tau) = 1 + [g^{(1)}(\tau)] \tag{1.10a}$$

$$g^{(2)}(0) = 1 + \frac{(\Delta n)^2 - \langle n \rangle}{\langle n \rangle^2} = 2 \tag{1.10b}$$

The value $g^{(2)}(0)$ shows that thermal light has large intensity fluctuations arising from the boson character of photons. The number of photons in a given mode is ruled by the Bose-Einstein distribution of black-body radiation:

$$p_{TL}(m) = \frac{\langle n \rangle^m}{(1 + \langle n \rangle)^{(m+1)}}, \tag{1.11}$$

being $\langle n \rangle$ the average number of photons in the mode. Therefore, the zero photon state is the one with the highest occupation probability.

2. Coherent light: A stabilized laser light is classically depicted as a wave with constant amplitude and phase, leading the first and the second-order correlation function value to unity. Actually a laser output amplitude appears extremely regular, because the fluctuations of its photon number is negligible on macroscopic scale respect to the average number of photons. In quantum framework, a laser can be represented by a coherent state $|a\rangle$, which is

7

an eigenstate of annihilation operator:

$$\hat{a}\ket{a} = a\ket{a}, \tag{1.12}$$

where a is a complex number.

As any other state, a coherent state can be expressed as a linear combination of Fock states according to the following equation:

$$\ket{a} = e^{-|a|^2/2}\sum_{n}\frac{a^n}{\sqrt{n!}}\ket{n} \tag{1.13}$$

The number of photons in a coherent state follows a Poisson distribution and therefore the probability of finding m photons in a given mode is:

$$p(m) = \frac{\langle n\rangle^m}{m!}e^{-\langle n\rangle}, \tag{1.14}$$

where $\langle n\rangle = \Delta n^2 = |a|^2$. In this case $g^{(2)}(0)$ is equal to unity. An intrinsic noise, $\Delta n^2 = \langle n\rangle$, is associated to a macroscopic laser source and it is called shot noise.

3. Squeezed light: Being a mode of the electromagnetic field in a cavity quantized as a harmonic oscillator, it can be described by two non-commuting operators, i.e. the electric field and vector potential or amplitude and phase. According to Heisenberg uncertainty principle, quantum mechanics allow the realization of squeezed states of light, where quantum fluctuations in one quadrature can be reduced (as compared with those of a coherent state) at the expense of enhanced fluctuations on the conjugate component. Therefore, squeezed light with decreased amplitude fluctuations must present an increase of phase noise. An ideal amplitude-squeezed source is one that delivers a regular stream of photons equally spaced in time. As a consequence, the fluctuations of the number of photons emitted by an amplitude squeezed source are weaker than those of a coherent state and they follow

a sub-Poissonian distribution. Applying equation 1.8 to a photon-number state:

$$g^{(2)}(0) = 1 - \frac{1}{n},\qquad\qquad (1.15)$$

being equal to zero for an ideal single-photon source ($n = 1$).

HBT INTERFEROMETER

Typically, the second order correlation function $g^{(2)}(\tau)$ is measured by the Hambury-Brown and Twiss interferometer, whose setup is depicted in figure 1.1.2. Incident light is divided by a 50-50 beam splitter and it is collected by two single-photon detectors. The coincidence events are recorded and the distribution of pairs of consecutive photons is obtained. The advantage of exploiting coincidences between two detector is that coincidences are insensitive to dead-time and after-pulses. In fact, using an ideal detector, anti-bunching would be easy to demonstrate: the stream of emitted photons is recorded with a time resolution better than the fluorescence time. With real photon-counting detector (e.g. SPAD), a period of blindness occurs after the measurement of one photon (dead-time) and spurious counts (after-pulses) can be produced by stray charges released upon the detection avalanche. Non-idealities in the detection stage destroy the photon statistic leading to the recording of a Poissonian distribution, even if photons are produced by a sub-Poissonian source. The second-order correlation function is in principle different from an histogram of coincidences. In fact it gives the distribution of all pairs of photons and not only of consecutive pairs. Nevertheless the two distributions are related and nearly equal for short delays allowing the evaluation of $g^2(0)$ by means of the HBT interferometer.
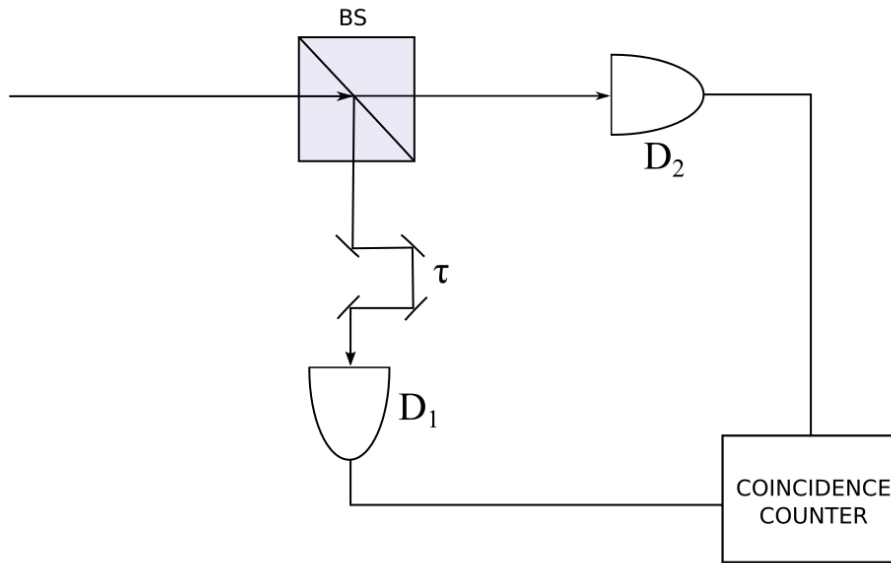
Figure 1.1.2: A schematic of the HBT interferometer. The incident light is divided by a 3dB beam splitter (BS) and detected by two single-photon detectors D_1 and D_2. The correlation of light intensities is measured varying the optical path length difference τ between the BS and the two detectors.

1.2   IMPLEMENTATION OF SINGLE-PHOTON SOURCES

1.2.1   IDEAL SINGLE-PHOTON SOURCE

An ideal single-photon source [7] has to fulfill the following requirements:

- **ON DEMAND PRODUCTION**: Each single-photon can be emitted at any arbitrary time defined by the user. The probability of emitting a single photon is 1, while the probability of multiple-photon emission is 0. Therefore, the emission quantum yield must be unity and the excited state of the emitter must be prepared with certainty.

- **INDISTINGUISHABILITY**: Subsequent photons have to be emitted in the same spatial mode and in the same coherent frequency wavepacket. This requirement must be satisfied in order to exploit quantum interference as

stated by Hong-Ou-Mandel effect. Two photon impinging at the same time on the two input ports of a balanced beam splitter interfere in such a way that they both exit from the same output port as depicted in Fig. 1.2.1. In fact, if the two photons are indistinguishable, a completely destructive interference occurs and the coincidences on the two output detectors drop to zero for zero delay. The shape of the dip is directly related to the power spectrum of the single-photon wavepacket. The spectrum of the source should be Fourier-transform limited and for a two-levels emitter its broadening is generally associated with:

1. Dephasing: The collisions of the emitter with the bath lead to the loss of coherence. The coherence time T_2 of the source is represented by the following equation:

$$\frac{1}{T_2} = \frac{1}{2T_1} + \frac{1}{T_2^*}, \qquad (1.16)$$

where T_1 is the fluorescence time and T_2^* characterizes the pure dephasing processes. In this framework, each photon can be represented as a short incoherent wavepacket emitted at random time during T_1, resulting in a reduction of two-photon interference dip to $T_2/2T_1$.

2. Spectral diffusion: Due to the fluctuations of the optical resonance frequency, two photons emitted in a time interval longer than the spectral diffusion time will be distinguishable: i.e. they differ in the central frequency.

- **REPETITION RATE**: It should be arbitrary fast and it is hopefully limited only by the temporal duration of the single-photon pulses.

- **REPRODUCIBLE SOURCES**: The possibility of working simultaneously with several photons is quite desired in quantum applications and thus it is preferable that a single-photon source is reproducible. Therefore, different sources should generate indistinguishable photons. The same result can
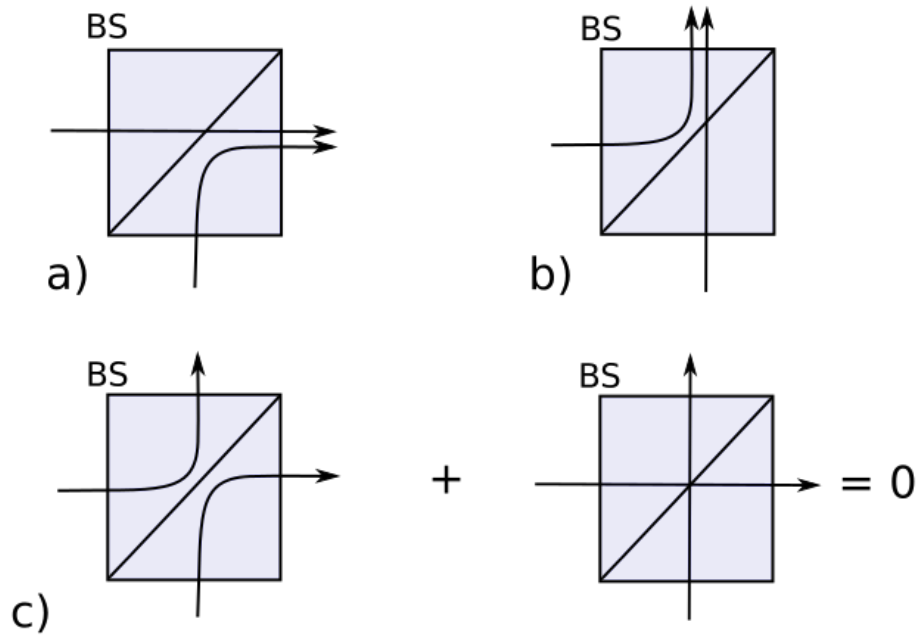
Figure 1.2.1: A schematic of photon coalescence effect. Two single-mode photons simultaneously enter in the two ports of a 3 dB beam splitter. They give rise to transmitted or reflected amplitude. If they are indistinguishable, the two paths in (c) and in (d) interfere destructively. Only paths (a) and (b) contribute to observed amplitudes and thus both photons emerge at the same output port.

be obtained storing indistinguishable photons emitted from a single-source and emitting them at the same time when required.

1.2.2 DETERMINISTIC SOURCES

There are a huge variety of systems that have been studied as on-demand single-photon sources. Most of them are composed by a single emitting nano-object, which is pumped into an excited state by an external control and spontaneously relax to a lower-energy state emitting a photon. Generally, in order to achieve high repetition rate and avoid excitation events with null emission, two conditions have

to be fulfilled:

1. The emission quantum yield of the system must be as high as possible. The emission yield of the nano-object can be increased placing it in a resonant cavity and exploiting the enhanced spontaneous emission through Purcell effect.

2. The excited state must be prepared with unitary probability after each emission cycle.

1.2.2.1 SINGLE ATOMS

Single-atom emitters [8] are designed to work in strong coupling regime, where the cavity enhances single-photon emission into a single spatial mode. The isolation, manipulation and trapping of single atoms require sophisticate and expansive setup. Atoms are first trapped into a magneto-optical trap and cooled in order to reduce collisions with residual gas, which cause dephasing and thus a broadening of the emitted spectrum. When the magneto-optical trap is switched off, gravity makes the atoms fall inside a high-finesse optical cavity, where an optical trap is activated. The atom is characterized by purely electronic eigenstates: two metastable ground states $|g\rangle$ and $|u\rangle$ and one excited state $|e\rangle$ in the so called Λ configuration. The transition of $|u\rangle \rightarrow |e\rangle$ is resonant with the pump laser pulse, while the resonance of the optical cavity is set close to the transition of $|g\rangle \rightarrow |e\rangle$. The atom-cavity system is characterized by a 3-level Hamiltonian: $|e, 0\rangle$, $|u, 0\rangle$ and $|g, 1\rangle$. The atomic state $|u\rangle$ can be transferred to $|g\rangle$ via stimulated Raman adiabatic passage (STIRAP [9]). During STIRAP, a single photon is generated in the cavity mode and leaves it through an output mirror. The final state $|g, 0\rangle$ is reached and emission is blocked until a recycling procedure is performed to bring the system back to the state $|u, 0\rangle$. If a single atom is trapped in the cavity, the source will never emit two or more photons at the same time. The emitted photons will present transform-limited wavepackets and will be in principle perfectly indistinguishable. Because atoms are all identical, single-atom emitters can be produced in quantity for a scalable system. Which are the limitations? Despite the high efficiency of

single-photons generation, the losses on exiting the system can cut down the emission probability to 0.05. Atom-based sources require to work at cryogenic temperature in ultra-high vacuum. Furthermore, the operation time is limited by the dwell time of an atom in a cavity mode.

1.2.2.2 SINGLE IONS

As for single atoms, the combination of involved eigenstates (in the Λ configuration) and multi-step excitation procedure (far-off resonant Raman scattering or small detuning STIRAP) inhibits multi-photon events from a single-ion. Furthermore, the strong confinement provided by radio-frequency ion trap ensures stable ion localization in the center of optical cavity and thus the isolation of a single emitter. The indistinguishability [10] between different pulses and sources is almost perfectly guaranteed; thus the scalability in the number of single-ion emitters is not an issue. Being strong coupling regime not straightforward for charged particles, an efficient collection of light is problematic. Moreover, the high spontaneous decay rates for the involved resonant transitions compete with the emission of radiation in the cavity mode lowering the probability of emitting a single photon during each pump cycle. The effect of such a drawback is enhanced by the not null probability that ions remain in the ground state at the end of the excitation pulse without emitting a single photon.

1.2.2.3 ORGANIC MOLECULES

Photon antibunching in condensed matter was first observed in a single-molecule system. The eigenstates involved in the emitting transition are not purely electronic, but they involve phonons and vibrations. In principle, they can be approximated by a three-level system: a singlet ground state $|S_0\rangle$, a singlet excited state $|S_1\rangle$ and a triplet intermediate state $|T_1\rangle$. Due to the presence of additional vibrational levels for each state, the single-photon emission presents a very broad spectrum. As long as the molecule is excited from $|S_0\rangle$ to $|S_1\rangle$ and radiatively decays to $|S_0\rangle$, a train of single-photons is generated. Unfortunately, when the molecule is trapped

in the dark state $|T_1\rangle$ (with low probability because it is forbidden by electric dipole rules), the emission rate drops and the anti-bunching is deteriorated on longer time scale. To overcome this issue, different solutions were proposed: the use of high intensity pulsed laser or the application of a strong sinusoidal electric field to shift the molecules absorption on and off the laser resonance. Despite molecular photo-stability is critical, operation time can be extended to hours with the appropriate engineerization of the material and working condition. Indistinguishability [11] is achievable between photons emitted by the same molecule exploiting the so-called zero-phonon line (ZPL), which characterizes the transition from the ground vibrational state of the ground to the lowest excited electronic state. Due to the strong dependence of molecules on their environment, further improvements are required to increase the number of identical sources. Cryogenic temperatures, even if not strictly necessary, are recommended to work with a Fourier-transform limited emission.

1.2.2.4 COLOR CENTERS

Defects inside an insulating inorganic material lead to the formation of localized electronic states and present intense absorption and fluorescence bands. The electronic wavefunctions and the photophysical properties of colour centers are comparable to those of organic molecules, but their photostability is much improved. Among the systems which present individual defects, diamond is deeply studied due to its mechanical stiffness and stability.

When one of the carbon atoms is replaced by a nitrogen and one of its neighbours is missing, a nitrogen vacancy (NV) colour center [12] is formed. The zero-phonon emission line is centered around 637 nm and the spectrum is broader than 100 nm. Furthermore, the presence of a dark state in the energy-system is responsible for a decrease in the emission rate and for bunching in the correlation function.

The nickel-nitrogen vacancy colour center [13] has an emission line around 800 nm and presents a spectral bandwidth of few nanometer, smaller than the one of the NV centers even at room temperature.

The spatial aberration and the small collection solid angle associated with high refractive index of diamond leads to a drop in single-photon collection efficiency and thus bulk diamonds have been replaced by diamonds nanocrystals, which are also easier to manipulate. Moreover, the associated background reduction leads to a decrease in $g^2(0)$. NV color centers are not identical and thus the scalability in the number of sources is limited. However, a tuning of the spectrum to make emitted photons indistinguishable can be performed applying an external electric field.

1.2.2.5 Quantum Dots

Semiconductor quantum dots [14] are tiny islands of low-band-gap semiconductor embedded in a high-band-gap semiconductor (e.g. InGaAs in GaAs). A typical procedure for the fabrication of quantum dots (QDs) exploits the process of Stranski-Krastanov growth, which allows the realization of uniformly sized three-dimensional structures. Small dots present discrete energy spectrum with few quantized levels for the holes and the electrons. In the weak-excitation regime, an exciton can be produced on-demand and the recombination of the trapped electron with the hole leads to the emission of a single-photon. The excitation (optical or electrical) efficiency is close to unity, but the emission efficiency is generally smaller. Using standard growth techniques, the QDs can be easily incorporated into a resonant cavity in order to increase the extraction factor and thus the emission rate. In fact, when the source frequency matches the cavity mode one, an enhancement of spontaneous emission due to Purcell effect [15] can be observed. In addition, the cavity mode directs the emission mode into a single spatial mode and an increase of collection occurs. A QD can also capture two electrons and two holes to form a bi-exciton state, which decays by radiative cascade emitting two photons with different energies. This effect can be exploited to produce polarization-entangled photon pairs [16], even if several arrangements must be employed to remove the polarization splitting in the emission cascade. Because of multiple-exciton lines, cryogenic temperatures are usually required in order to

work with single-photons. Furthermore, at higher temperature the exciton can escape towards the wetting layers or the substrate. In addition, at low temperatures the emission spectrum is closed to be Fourier-transform-limited. The indistinguishability between different QDs is not particularly high due to the hosting uncontrolled solid-state matrix. Each QD is thus different from the others and to achieve systems scalability a fine tuning of single emitters is necessary.

1.2.3 PROBABILISTIC SOURCES

Currently, the most widely employed single-photon sources for quantum information science are probabilistic sources based on nonlinear phenomena: i.e. spontaneous parametric downconversion and four-wave mixing. As a result of the nonlinear interaction between a medium and an excitation laser, it is possible to generate correlated pairs of photons, which can be exploited to create pseudo-single photon states. A photon of the pair is used as a trigger for detecting its twin: the heralding photon of the pair heralds the existence of the heralded photon. Due to the statistical nature of the photon-pair production process, this kind of source is not on-demand and most of the time no photons are produced. Furthermore, the probability of generating multiple-pairs is not negligible. Even if the specifics of photon number distribution is dependent on the details of the source, an inspect of the output state of spontaneous parametric downconversion process can help to understand the general behaviour of probabilistic sources:

$$|\Psi_{SPDC}\rangle = \sqrt{1 - |\lambda|^2} \sum_{0}^{\infty} \lambda^n |n, n\rangle, \qquad (1.17)$$

where $|\lambda|^2$ is proportional to the laser pump power and $|n\rangle$ is the n-photon Fock-state. The probability of generating n-photon pairs is given by $P(n) = (1 - |\lambda|^2)/|\lambda|^{2n}$, while the probability of creating $(n+1)$ photon pairs is given by $P(n+1) = |\lambda|^2 P(n)$. Since the ratio $P(n+1)/P(n)$ increases with $|\lambda|$, the pump power and the average single-pair production must be kept below unity to avoid multiple-pair production. Decreasing the mean number of pairs generated, the second-order correla-

tion function $g^{(2)}(0)$ of the heralded source can be made arbitrary close to zero. Therefore, probabilistic sources present a trade-off between brightness and purity $g^{(2)}(0)$. The exploitation of number-resolving-photon detectors, which allow to distinguish multiple-pair generation from single-pair generation, represents a smart strategy to bypass the above trade-off. Another way of dealing with probabilist emission is to couple the heralded source with a photon storage mechanism; this combination will move the pair source toward deterministic operation. In regards to emission rate and $g^{(2)}(0)$, losses in the photon-path must be considered since they perturb the photon number distribution of the source: i.e. the single-pair emission is more sensitive to losses with respect to multiple-pair one. An heralded photon can be lost during its propagation leading to a null measurement. Stray light or dark counts can behave as false heralds resulting in a void detection. In addition, unheralded photons will be emitted due to losses in the heralding channel. To overcome this issue the heralded channel should be opened only when triggered by a herald [17].

1.2.3.1 Spontaneous Parametric Down Conversion

The interaction of a pump laser pulse with a non-centrosymmetric $\chi^{(2)}$ nonlinear media can lead to the conversion of the incident pump photon into two lower energy photons. The two daughter photons, which are generated simultaneously [18], are called signal and idler. In this process called spontaneous parametric downconversion (SPDC) photon energy and momentum conservation (Fig.1.2.2) impose:

$$\begin{cases} \hbar w_p = \hbar w_s + \hbar w_i \\ \hbar \vec{k_p} = \hbar \vec{k_i} + \hbar \vec{k_s} \end{cases} \tag{1.18}$$

where the indices p, s, i stand for the pump, signal, and idler photons. The momentum conservation law is also called "Phase-Matching" condition.

If the downconverted photons have equal frequency ($w_i = w_s = w_p/2$), the process is called degenerate. Otherwise, it is said to be nondegenerate. In this case, a
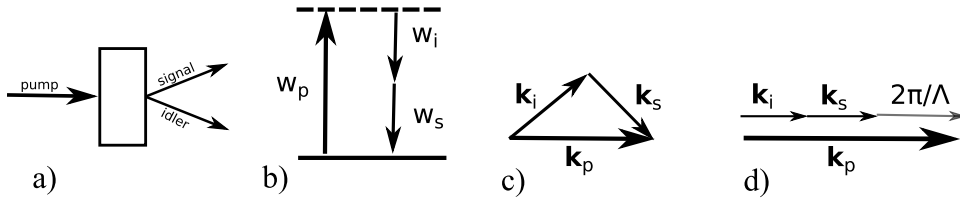
Figure 1.2.2: (a) Schematic of non-collinear SPDC. A pump photon interacts with a nonlinear $\chi^{(2)}$ material and it is converted into an idler and signal photon. (b) Energy conservation condition; (c) Phase-Matching condition and (d) Quasi-Phase-Matching condition

continuum of other energy and momentum pairs is achievable, determined by the dispersion relations of the material under the constraints of the above conservation laws.

For SPDC using bulk nonlinear crystals, there are two types of birefringent phase-matching:
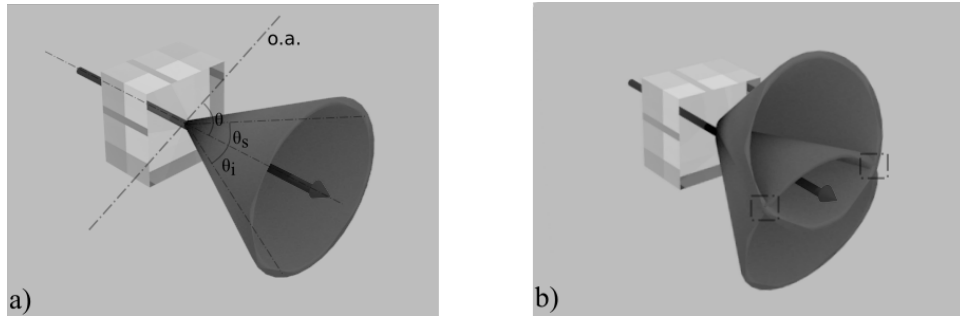
Figure 1.2.3: Schematic of angular phase-matching in bulk crystals. The pump field direction and the optical crystal axis (o.a) form an angle θ. The downconverted photons emerge at angles θ_i and θ_s. a) In Type I configuration the signal and idler photons have the same polarization. b) In Type II configuration they have an orthogonal polarization. Photons emerging from the intersections are naturally entangled [19].

- TYPE I: the daughter photons have the same polarization orthogonal to the one of pump photon as depicted in Fig. 1.2.3a. In the case of degenerate SPDC, the pair of photons emerges in a cone centered on the pump beam and whose opening angle depends on the angle between the pump direction and the optical axis of the crystal.

- TYPE II: the downconverted photons have orthogonal polarization and thus they are emitted in two cones, one ordinary and the other extraordinary polarized. Varying the incident pump angle, the two cones tilt towards the pump and intersect along two symmetric directions as represented in Fig. 1.2.3b. Where the two cones intersect, a Bell entangled state is obtained:

$$|\psi\rangle = \frac{|H_1, V_2\rangle + e^{i\varphi}|V_1, H_2\rangle}{\sqrt{2}}, \qquad (1.19)$$

where the phase term is induced by crystal birefringence.

In order to obtain photon pairs with desired wavelength and phase-matching properties, the crystal can be engineered through periodic poling [20]. This technique employs a periodic reversal of the ferroelectric polarization to induce a periodic inversion of the sign of the second order nonlinear coefficient allowing to achieve phase-matching where it is otherwise impossible [21]. The phase-matching condition thus becomes:

$$\vec{k}_p = \vec{k}_i + \vec{k}_s + \frac{2\pi}{\Lambda} \cdot \vec{u}, \qquad (1.20)$$

being Λ the poling period and $\vec{u}$ the unitary vector along the propagation axis. This condition is called "Quasi-Phase-Matching" [22] and it is represented in 1.2.2d. This additional degree of freedom allows to generate twin photon with the same polarization of the pump photon also in the collinear configuration (Type 0). Another advantage of this configuration with respect to birefringence phase-matching is that it permits to exploit the largest nonlinear coefficient in the materials. For example, in $LiNbO_3$ the d_{33} coefficient is thus available leading to an increase of photon-pair yield. In addition to QPM, a further improvement to bulk SPDC is

the use of waveguides. In fact, in bulk SPDC, as represented in Fig. 1.2.3, the photon pairs are typically generated in multimode cones surrounding the pump laser. Due to the presence of different spatial modes, a post-generation modal filtering is required. The implementation of waveguiding structures in $\chi^{(2)}$ materials partially resolves this issue, since waveguide SPDC sources can provide a single transverse mode beam. Furthermore, waveguides allow to confine the pump beam over the whole interaction length, rather than only near the focal point. As a consequence, an improvement of conversion efficiency, up to four order of magnitude over the bulk birefringent phase-matching configuration, is achievable [23]. In addition, they pave the way to the integration of SPDC sources and other optical elements into small-scale devices.

1.2.3.2   FOUR WAVE MIXING

Four-wave mixing (FWM) is the dominant nonlinear process in centrosymmetric materials (e.g. glass), which do not present second order nonlinearity $\chi^{(2)}$. The $\chi^{(3)}$ nonlinear response of glass can lead to the spontaneous conversion of two pump photons into a correlated pair of photons, known as the signal and the idler, when the constraints of energy and momentum conservation are satisfied. Notwithstanding the low value of $\chi^{(3)}$ nonlinearity in glass, the long interaction length achievable in optical fibers allows to efficiently generate photon pairs with FWM [24]. Obviously, a collinear geometry is required to work with optical fiber. The spectral properties of the generated photon pairs are strongly dependent on the dispersion properties of the fiber. Working near the zero-dispersion wavelength of the fiber, it is possible to obtain both degenerate (even close to the pump wavelength) and strongly nondegenerate daughter photons. Photon pair generation has been demonstrated also in photonic crystal fiber, which ensures higher flexibility (i.e. broad tunability of phase-matching from visible to C-band) exploiting the controlled modification induced on dispersion by the proper design of the fiber structure [25]. Since the generated photons are generated in the fundamental mode of the fiber, they can be efficiently coupled into standard single mode fiber.

Exploiting FWM, heralded single photon sources have also been demonstrated in dispersion shifted fibers, birefringent single-mode fibers [26] and silicon-on-insulator (SOI) waveguides [27]. In addition, two-photon states and in particular, polarization-entangled photon states can be generated by employing fiber-based sources. A limitation to brightness and purity of FWM based-source is the so-called Raman scattering. Throughout its propagation, a pump photon can be inelastically scattered by the glass leading to the emission of a phonon and a red-shifted photon. When the wavelength of the Raman scattered pulse overlaps with the wavelength of the idler, an increase in the background count rates occurs. Different strategies can be exploited to mitigate the effect of Raman scattering [28, 29].

1.2.4 APPLICATIONS

A major drive in the development of compact, efficient and reliable single-photon sources has been provided by several exciting applications, which rely on the quantum-mechanical effects related to Fock states (i.e squeezing and entanglement). Although other physical systems present these quantum properties, photons are ideal candidates in data transmission and metrology, since they exhibit very low decoherence. Here we report few examples of single-photon source applications.

QUANTUM INFORMATION

Quantum-information science deals with the encoding, manipulation and measurement of information using quantum-mechanical objects. It could allow to perform computational tasks and simulation more efficiently than in the case of classical computing. The fundamental unit in quantum information is the qubit: a quantum two-level system prepared in a coherent superposition of its eigenstates $|0\rangle$ and $|1\rangle$.

$$|\psi\rangle = \alpha |0\rangle + \beta |1\rangle , \qquad (1.21)$$

where α and β are complex amplitude. Due to their ability to transport information over long distances, their negligible decoherence and the possibility of being encoded in several degrees of freedom (polarization, time bin or path [30]), the choice of photons as qubits seems an excellent one. However, the photon-photon interaction is very weak and the realization of logic gates for quantum computation scheme, in which two qubits have to strongly interact, had appeared as a really challenging task until the discovery of Knill, Laflamme and Milburn in 2001 [31]. Knill et al. showed that single-photon sources, passive linear optics and single-photon detectors are sufficient for implementing reliable quantum algorithms. In their scheme, the photons must undergo quantum interference on beamsplitters, which implies that they must be indistinguishable. Furthermore, very high efficiencies are needed. In fact, it has been successively shown that if all the other components are perfect, quantum computation is possible if the overall efficiency of source and detector is greater than $2/3$ [32].

QUANTUM CRYPTOGRAPHY

Quantum Key Distribution (QKD) is a secure method for the exchange of a secret key between two distant partners, Alice and Bob. Its safety is guaranteed by the impossibility of measuring an unknown quantum-mechanical state without modifying it. Thus, in an ideal experimental system, an eavesdropper, traditionally referred to as Eve, cannot intercept Alice and Bob's secret key without introducing detectable errors in the communication. The ideal scheme of QKD demands single photons, since the presence of multiple photons in the channel can compromise the security of the communication by allowing Eve to gain information [33]. The first protocol for QKD proposed by Bennett and Brassard (BB84) [34] has been progressively modified in order to relax the single-photon requirement and reduce the potential leakage of information to Eve. Although these schemes, such as those based on decoy states[35] and privacy amplification[36], have shown their effectiveness even with attenuated laser, long distance key-sharing, which requires quantum repeaters[37], heavily relies on single-photon.

QUANTUM METROLOGY

The Heisenberg uncertainty principle $\Delta A \Delta B \geqslant \frac{1}{2}|\langle[A, B]\rangle|$ between the standard deviation of two arbitrary observables has a built in degree of freedom, which is unexploited in classical approach. In fact, one can squeeze the standard deviation of one observable provided one stretches that of the conjugate one. This allows to define an optimal measurement strategy for a desired quadrature.

Using a coherent state with an average number N of photons, the weakest measurable absorption of a medium is determined by shot noise. Working with an ideal single-photon source, the number of photons sent into the absorber is well-known and fixed leading to a Binomial distribution of the detected counts and a reduction of the associated standard deviation. The combination of a perfect single-photon source and a perfect detection would give access to the measurement of arbitrary small absorptions [7].

Exploiting quantum entanglement and in particular a NOON state [1] it is possible to overcome the Rayleigh diffraction limit. Classical lithography is limited to writing features of a $\lambda/2$ size or greater, where λ is the optical wavelength. The resolution limit for a NOON state is reduced to $\lambda/2$N [38]. Furthermore, the use of a NOON state allows to measure a phase with a precision of $1/$N outperforming the $1/\sqrt{N}$ precision limit possible with N unentangled photons [39].

---

[1] A NOON state is a many-body entangled state:

$$\varphi_{NOON} = \frac{|N\rangle_1 |0\rangle_2 + e^{iN\theta} |0\rangle_1 |N\rangle_2}{\sqrt{2}}, \tag{1.22}$$

which represents a superposition of N particles in mode 1 and 0 in mode 2 and viceversa. Multi-photon states can be created by interference of indistinguishable single-photons at a beam splitter.

2

Femtosecond Laser Micromachining

In this chapter femtosecond laser direct writing technique is presented. In section 2.1 the interaction between a femtosecond laser pulse and a dielectric material is introduced. In section 2.2 the main parameters involved in the waveguide fabrication process will be described. Section 2.3 contains an overview on the principles and methods for the realization of waveguides in crystalline structure.

INTRODUCTION

The optical properties of a small volume inside a transparent substrate could be modified in a permanent way by tighly focused femtosecond laser pulses : this demonstration by Davis et al. in 1996 [40] paves the way to femtosecond laser micromaching (FLM) of transparent materials. The relative translation between the substrate and the focus of the laser beam allows direct optical waveguide writing due to the capability of inducing an increase of the refractive index localized in the focal volume. The advantages of this technique over other competing processes are:

- RAPID PROTOTYPING: FLM is a single-step and maskless fabrication technique. It doesn't require any clean room facility. Due to the simple fabrication setup it allows rapid prototyping and small scale production with a significant cost reduction and process speed-up.

- FLEXIBILITY: Relying on the nonlinear nature of FLM and tailoring the writing parameters, in principle almost any type of transparent material can be processed, i.e. glasses, crystals and polymers.

- 3D GEOMETRY: Due to the nonlinear interaction between the femtosecond laser pulses and the processed material, the irradiated volume is limited around the focal volume of the laser beam and so it's possible to write at arbitrary depths inside the substrate. A degree of freedom is thus added with respect to other fabrication techniques and therefore innovative configurations and structures are allowed.

2.1 FEMTOSECOND LASER INTERACTION

IN BULK DIELECTRICS

FLM is based on the nonlinear interaction of a train of femtosecond laser pulses with a transparent material. A strong laser beam is focused beneath the surface of the substrate and, if the photon energy E = hν is less than the bandgap energy E_g between the valence and the conduction band, linear absorption phenomena are inhibited and nonlinear photoionization occurs promoting an electron from valence to conduction band. The process can be divided in three steps: generation of free electron plasma, energy relaxation and material modification.

a)   b)   c)
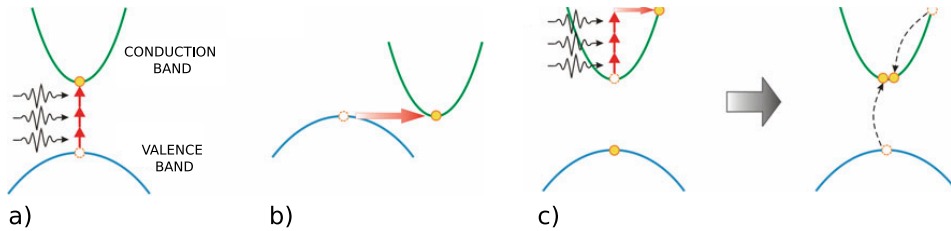
Figure 2.1.1: Schematic of the interaction between a femtosecond laser pulse and a transparent material. (a) Multiphoton absorption (b) Tunneling ionization (c) Inverse Bremmstrahlung and avalanche photoionization. The image is taken from [41]

Free electron plasma formation is mainly induced by two mechanisms: multiphoton absorption and tunneling ionization. In the former process, typically in the low laser intensity and high frequency regime, m photons
(mhν > E_g) are simultaneously absorbed by a valence electron allowing its promotion to conduction band. At higher intensity the strong field applied to the material can induce a distortion of the band structure causing a reduction of the potential barrier between valence and conduction band and allowing the band to band tunnelling of an electron. Evaluating the Keldysh parameter [42] for typical waveguide writing condition, it is possible to deduce that both processes contribute to nonlinear ionization. The seed of free electrons is thus sprouted and

it can be amplified through avalanche photoionization process. The free electron can absorb light through inverse Bremmstrahlung and thus acquire several photons in a linear sequential way until its energy exceed the bandgap energy E_g. The hot electron is now ready to excite a bound valence electron through impact ionization and promote it in the conduction band. As long as the laser is present and strong enough, the process repeats causing the formation of an electron avalanche. Avalanche ionization contributes in the growing of free electron density until the plasma frequency gets close to the laser frequency v and thus the remaining energy of the laser pulse is transferred to the plasma through free carrier absorption. In a time-scale of 10 ps the electron-ion plasma relaxes and the energy is transferred to the lattice inducing a modification of the material in a microsecond time-scale. Different physical phenomena (e.g. densification [43], colour center formation [44], ion exchange/migration effects [45]) are involved in the alteration of the optical properties of the substrate, but the precise role of each of them is strongly dependent on the material properties and the exposure parameters. In general, it is possible to identify three main regimes of material modification. Working with low pulse energies a smooth and isotropic refractive index increase [46, 47] can be obtained and this modification fits the requirements for the realization of optical waveguides. At higher pulse energies birefringent refractive index change and the formation of nanogratings can be observed [48]. A further increase in the pulse energies leads to the generation of micro-explosions and the formation of empty voids inside the substrate[49].

Using sub-picosecond pulses entail two advantages: deterministic breakdown and the decoupling of absorption process to lattice heating process. For longer pulses it is difficult to reach the pulse peak intensity required to trigger nonlinear photoionization, which provides seed electrons for avalanche ionization and allows plasma generation in a deterministic way around the focal volume. In fact, the creation of the free electron plasma is still possible, but the seed is provided by thermally excited electrons or by the presence of impurity or defect states inside the material. Their concentration is typically low and their number fluctuates in time and space inducing stochastic breakdown through avalanche ionization.

28

Furthermore, since the temporal scale of plasma relaxation is in the order of 10 ps, the free electron carriers formation and the lattice heating processes are temporally decoupled leading to a more precise micromachining.

2.2 WAVEGUIDE WRITING PARAMETERS

2.2.1 FOCUSING

Incident femtosecond laser pulses are focused inside the substrate with an external system of optics in order to achieve a small focal spot and trigger nonlinear absorption. Chromatic and spherical aberration cause a deviation of the intensity distribution near the focus and can be partially compensated using a microscope objective. In the approximation of linear propagation and null spherical aberration, the spatial intensity profile of a femtosecond laser beam can be represented in Gaussian optics. The diffraction-limited minimum waist radius w_0 and the Rayleigh range z_0 of the beam are given respectively by:

$$w_0 = \frac{M^2 \lambda}{NA\pi} \tag{2.1}$$

$$z_0 = \frac{nM^2 \lambda}{NA^2\pi}, \tag{2.2}$$

being M^2 the Gaussian beam propagation factor, λ the laser free space wavelength, NA the numerical aperture of the focusing objective and n the refractive index of the glass. An objective with an higher NA allows theoretically to obtain a tighter and less elongated focus. The depth of the focus beneath the substrate surface is another key parameter in waveguide fabrication. In fact, an additional contribution in spherical aberration is introduced by the index mismatch at air/glass interface and it is translated into a strong depth dependence of device properties. This effect is stressed for higher NA objectives, but it can be limited using an oil-immersion objective due to the reduction of the refractive index mismatch for the stacked structure. However, this kind of objectives has a limited working distance

and available depth range. Another solution is represented by dry objectives with collars that enable the correction of spherical aberration at different processing depths.

In the choice of working depth the effect of nonlinear propagation should be taken into account and it can be represented through the nonlinear refractive index n_2 of the material. An intense laser beam is focused inside a dielectric with a strength dependent on the peak power. If the peak power exceeds the critical power for self-focusing:

$$P_c = \frac{3.77\lambda^2}{8\pi n_0 n_2};$$ (2.3)

the pulse collapses to a focal point, nonlinear ionization process is activated and free electron plasma is produced. The free electron plasma behaves as a diverging lens balancing the Kerr-lens self-focusing and causing the formation of light filamentation. This effect leads to the creation of elongated and distorted focal spot and makes writing of waveguide in nonlinear media very challenging (i.e. chalcogenide glasses [50], heavy metal oxide [51], silicon crystals [52]).

2.2.2 WRITING CONFIGURATION

Two standard configurations [53] can be identified for the fabrication of optical waveguides through FLM:

1. LONGITUDINAL: In this geometry, the sample is translated along the incident beam propagation direction. Therefore, the realized waveguide shows an intrinsic cylindrical symmetry due to the transverse symmetry of the Gaussian intensity profile of the fabrication beam. The main drawback of this configuration is that the processing length is limited by the working distance of the employed objectives.

2. TRANSVERSE: In this configuration, the sample is translated orthogonally to the beam propagation direction. The waveguide cross-section is strongly asymmetric depending on the shape of the focal spot, in particular on the ratio between the Rayleigh range z_0 (depth of the focus) and beam waist w_0

(half of the focus width). The elliptical cross section leads to an intrinsic waveguide birefringence and the supported guided modes couple with less efficiency to standard optical fibers. In order to obtain a symmetric cross section, beam shaping techniques or multiscan writing approach should be adopted. In principle, the limitation in the waveguide's length is removed (bounded only by working area of the sample translation stages and propagation loss inside the substrate) with an huge increase in design flexibility.

2.2.3 REPETITION RATE

The repetition rate [54] of the pulse train is a crucial parameter in waveguide fabrication with FLM and it is possible to classify two different processing regimes:

In the low repetition rate regime (<100 kHz) the material modification is almost completely determined by the interaction with a single femtosecond laser pulse. In fact, the heat piled in the focus is totally dissipated through thermal diffusion before the next pulse arrival. As a consequence the shape of modified region matches the shape of the irradiated focal volume and the waveguides written in the transverse geometry exhibit an asymmetric (elliptical-like) cross sections. Furthermore, the low repetition rate allows only low processing speeds (around 10-100 μm/s) entailing an increase of the overall fabrication time. Despite these disadvantages, this regime is widely used in waveguide fabrication because of the widespread availability of regeneratively amplified Ti:Sapphire lasers at 800 nm, which produce highly energetic femtosecond laser pulses with 1-200 kHz repetition rate.

Heat accumulation effects arise when the repetition rate is increased up to tens of MHz in order to make the time between two consecutive pulses shorter than the heat diffusion time (around 1 μs). Therefore the heat deposited in the focal volume does not have time to diffuse away and pulse overlap induces thermal accumulation effects, which allow to obtain cylindrically symmetric waveguides without the need of beam shaping techniques due to isotropic heat diffusion. Annealing and decreased thermal cycling related to high-repetition rate and high local tem-

perature increase allow to fabricate more uniform and symmetric waveguides with benefits both on the propagation losses and on the coupling losses to optical fibers. Moreover it is possible to increase the writing speeds up to 50-100 mm/s. Femtosecond laser oscillators without amplification stage are typically employed and so only low energy pulses are available. In order to reach the threshold intensity for nonlinear absorption, tight focusing is required and the use of high-numerical aperture oil-immersion objectives allows to fabricate structures only in the close proximity to the surface.

An intermediate regime (from hundreds of kHz to few MHz) can be observed employing Yb-based laser systems. These sources deliver femtosecond laser pulses with few μJ pulse energy and thus tight focusing is no longer required. Long working distance objectives can be employed allowing to completely exploit the 3D capabilities of FLM. In this regime, due to the combination of energetic pulses and thermal effects, higher refractive index contrast waveguides can be fabricated with high processing speeds and with uniform and symmetric structure.

2.2.4   BEAM SHAPING AND MULTISCAN TECHNIQUES

Beam shaping and multiscan techniques have been developed to fabricate waveguides with symmetric cross-section, even in transverse writing configuration and in the low-repetition rate regime. Since the waveguide cross-section is directly related to the spatial distribution of the induced electron plasma in the single-pulse interaction regime, beam shaping techniques rely on molding the inscription laser beam to control the corresponding cross-section.

The first technique [55, 56] employs a cylindrical telescope before the focusing objective exploiting its demagnification ratio to adjust the beam waist ratio and varying the position of the second cylindrical lens to tune the astigmatic difference.

In the slit beam shaping technique [57, 58] a micrometer controlled adjustable slit is placed in front of the focusing lens and is orientated along the sample translation direction allowing the reduction of the NA of the focusing in the plane perpendicular to waveguide axis. A change in the NA of the focusing is directly related

to a modification of the focused beam waist and exploiting this effect a beam waist ratio of ~ 10 is achievable, which is the estimated value for the fabrication of a symmetric waveguide cross-section.

Previous techniques work with a fixed waveguide cross-section along a fixed sample translation direction forbidding symmetry conservation for bended structure. A possible solution is represented by the replacement of the cylindrical telescope or the slit with a computer controlled active optics (e.g spatial light modulator and deformable mirror [59]). This arrangement allows to maintain symmetric cross-section waveguides even changing sample translation direction by synchronizing the phase and the amplitude profile of the laser beam with the sample translation. Another solution is the so called spatialtemporal focusing (STF) technique [60], which allows the control of the focal Rayleigh range independently of the focus beam waists and translation direction. Forcing spectral chirp before the objective lens and exploiting the gradient of the temporal focusing induced by pulse duration stretching, it is possible to create a spherical peak E-field distribution of the focus in the material.

The greatest flexibility in controlling the waveguide cross-section is achievable through multiscan technique [61, 62]. The single scan asymmetry is corrected by scanning the sample multiple times (around 20 for single mode waveguide) slightly varying the sample position. The combination of multiple material modifications allows to obtain an overall square and symmetric cross-section. Furthermore the use of this technique is not limited to single pulse regime, but it has also been employed in the previously described intermediate regime.

As previously stated, symmetric waveguide profile can be obtained in the transverse writing geometry exploiting isotropic thermal diffusion induced by thermal accumulation in intermediate/high-repetition rate regime, even without resorting to any beam shaping technique.

2.2.5 OTHER PARAMETERS

In addition to the previous parameters and techniques, the optimum processing window for waveguide fabrication in a given material is dependent on a lot of other factors. Translation speed influences the total energy deposited per unit of volume at a fixed pulse energy and it affects the achieved refractive index modification. The spatial distribution of the energy density in the focal volume is strongly affected by pulse duration through nonlinear pulse propagation process. The wavelength [63] of the incident laser beam is another parameter that should be taken into account in the fabrication process due to its strong influence on the order of multiphoton absorption in high bandgap materials. The laser-substrate interaction can be influenced by the writing direction due to a pulse front tilt in the incident beam according to the so-called quill effect [64]. Also the incident writing polarization [65] should be weighed in the definition of the fabrication procedure.

2.3 FABRICATION IN CRYSTALLINE MATERIALS

This section will provide an introduction on FLM in crystalline media, which are very interesting materials for integrated optics applications due to their unique properties, such as birefringence and high nonlinear response.

2.3.1 CRYSTALS MODIFICATION

The interaction of femtosecond laser pulses with regular crystalline lattice is strongly different than the one with amorphous structures. In fused silica the modification of the exposed material is mainly related to its densification. The rapid cooling of the melted glass in the focal volume freezes it in the high temperature state leading to an increase of the density and thus of the refractive index. In principle, a perturbation of an ordered crystalline structure is followed by a reduction of its density in the modified region. The morphological changes induced by the irradiation of crystals can be classified into two types. The first type is characterized by a weak

modification at the focal volume and by an increase of the extraordinary refractive index. After its first observation in $LiNbO_3$, the origin of this kind of modification was deeply investigated. Burghoff et al. [66] associated this change to the combined effects of defects in the crystalline lattice and the ferroelectric nature of $LiNbO_3$. Lattice defects lead to a reduction of spontaneous polarization P_S. In general, P_S is related to a decrease of the refractive indices due to the electro-optic effect according to the following relations:

$$\delta n_o = -\frac{1}{2} n_o^3 g_{13} P_S^2 \qquad (2.4a)$$

$$\delta n_e = -\frac{1}{2} n_e^3 g_{33} P_S^2, \qquad (2.4b)$$

where g is the quadratic electro-optic coefficient. Therefore, a reduction of spontaneous polarization results in an increase of n_e and n_o. This effect is counterbalanced by an expansion of the unit cell and thus a reduction of the refractive index. At low laser fluence, the lattice structure is preserved and the volume increase remains negligible allowing the realization of a positive extraordinary refractive index change. Being the effect of spontaneous polarization reduction smaller for n_o, a positive variation of the ordinary refractive index has never been observed. It is important to notice that isolated point defects can be annealed at temperatures around 200 °C. Stronger perturbation makes the volume change the dominant mechanism leading to a decrease of both refractive indices in the irradiated region. A stress field is induced in the region surrounding the exposed volume leading to an increase of the refractive index. This modification of the material is typically called Type II configuration and has been reported in a number of crystals. This approach allows the fabrication of waveguides exploiting the lateral areas of the tracks, which are characterized by an increased refractive index. Further explanation on waveguide geometries in crystals is provided in the following paragraph.

2.3.2 WAVEGUIDE CONFIGURATIONS

According to Chen et Vàzquez de Aldana [67], a different classification of FLM waveguides in crystalline materials is introduced. In this case, waveguides are not classified by the sign of the refractive-index change, but by the disposition of the induced tracks.
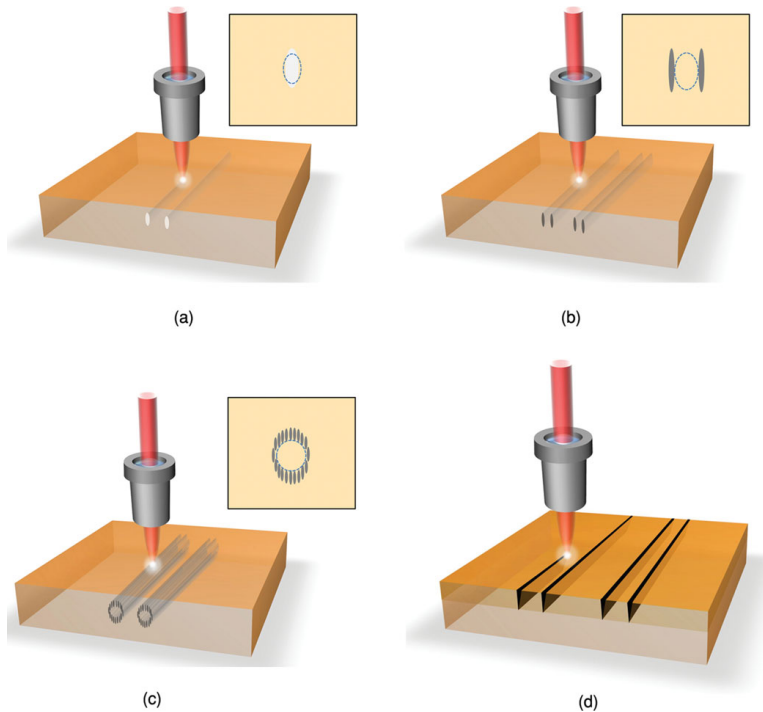
Figure 2.3.1: Schematic of the different fabrication configurations of waveguides in crystals through FLM: (a) Type I (Directly written waveguides) (b) Type II (Stressed-induced waveguides) (c) Type III (Depressed cladding waveguides) (d) Type IV (Ablated ridge waveguides). In the insets the cross-sections of the waveguides are sketched, where the shadows are the irradiated regions and the dashed lines delineate the waveguide cores. The image is taken from [67]

- Type I : In this configuration the guiding structure is directly fabricated in the exposed region. A positive refractive-index change ($\Delta n > 0$) is induced

in the irradiated focal volume by femtosecond laser writing. Although an index increase is very common in amorphous material, the mechanisms seem more complex in crystals and Type I modifications have only been obtained in few materials (LiNbO$_3$ [68, 69], ZnSe [70], Nd:YCOB [71]). Furthermore, the positive Δn can be obtained only along a particular axis supporting only one polarization direction. Another drawback of Type I waveguides is the lack of thermal stability: thermal deterioration occurs working at high temperature limiting their use in high-power applications. Since the interaction with femtosecond laser pulse is usually related to a strong modification of the focal volume, the destruction of the periodic lattice structures in the waveguide core can occur leading to a degradation of the associated bulk properties, such as nonlinear response. However, the bulk features can still be maintained with the proper choice of the processing parameters.

- Type II : The femtosecond laser pulses - crystal interaction produces a negative refractive-index modification in the exposed focal volume caused by the lattice expansion and the resulting local density reduction. The region surrounding the track typically present a slight increase of the refractive index due to stress-induced effects. Exploiting these properties, the waveguide core is typically located in the region between two highly damaged tracks following the so-called "double-line" or "dual-line" approach [66]. Since the waveguide core is not directly affected by femtosecond laser pulses, the bulk properties [72] are preserved. Type II waveguides can be realized in a broad set of crystals, generally support both horizontal and vertical polarization and they survive treatments at moderately high-temperature.

- Type III : In this configuration [73] the waveguide core is confined inside a quasi continuous low-index potential barrier wall, composed of a number of near damaged tracks ($\Delta n < 0$ as in Type II configuration). The quasiclosed cross-section of the depressed cladding waveguides can be engineered adjusting the arrangement of the tracks in order to support single mode (or highly multimode) guidance from visible to mid-IR wavelengths for both TE and TM polarizations. Furthermore, it is possible to obtain circular cross-section waveguides, which couple well with optical fibers.

- Type IV : High-intensity femtosecond laser pulses can be employed to etch crystals in selected regions in order to produce ablated ridge waveguides [74] on planar waveguide layer, which can be produced by other techniques. Postablation treatment is required to reduce the high roughness of the sidewalls and the resulting losses. A multiscan configuration can be used to further reduce sidewall roughness.

3

Experimental Setup

The experimental techniques and methods employed during the work described in this thesis are disclosed. Section 3.1 deals with the presentation of the setup used for the realization of the integrated photonic devices. In Section 3.2 the explanation on how to characterize the produced waveguides is explained.

3.1 FABRICATION SETUP

The experimental setup used to fabricate the optical circuits presented in this thesis is sketched in Figure 3.1.1. A femtosecond pulsed laser beam at 1030 nm is generated by a cavity-dumped mode-locked oscillator and it is carried by a system of dielectric mirrors to the machining area. Here, the writing beam is focused by a microscope objective inside the sample, which is glued above a three dimensional, computer driven, linear motion system. A precise setup alignment in the transverse fabrication geometry is achievable by a set of mirrors and a gimbal-based adjuster (GM100, Thorlabs) mounted on the translation stages.
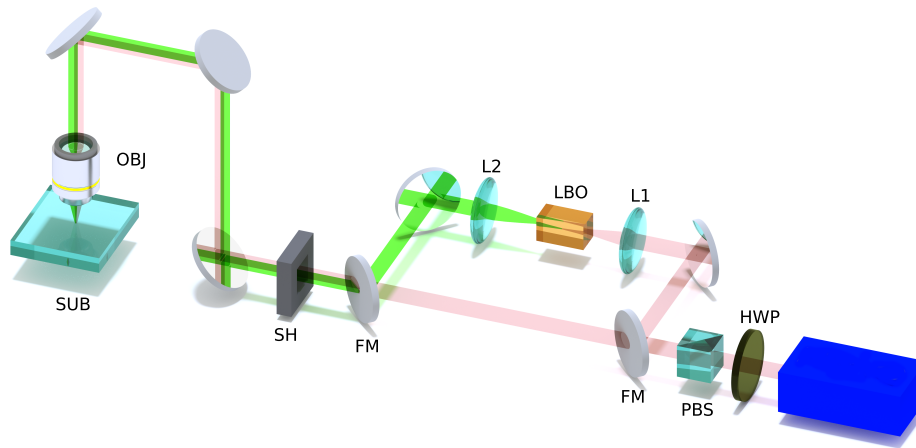
Figure 3.1.1: Schematic of the fabrication setup. A femtosecond laser beam at 1030 nm is delivered to a three dimensional high-precision translation stage, where the processing substrate (SUB) is fixed. The beam is tightly focused inside the material by means of a microscope objective (OBJ). The laser power can be controlled through a Glenn-Thomson polarizer cube (PBS) and a halfwave plate (HWP), while a mechanical shutter (SH) synchronized with the motion system allows a fast laser switching. Two flip mirrors (FM) permit to deviate the laser beam to a second harmonic generation stage (SHG) allowing to perform the fabrication process at 515 nm wavelength. Here, a 15 mm focal lens (L1) focuses the beam into a temperature controlled lithium triborate crystal (LBO) and the generated light is collimated by a 30 mm focal lens (L2). The image is taken from [75]

To obtain a precise and reproducible setting of the fabrication frame of reference, a CCD camera is used to collect the collimated back-reflected light of the laser beam when it is focused on the substrate surface. A mechanical shutter (SH05, Thorlabs) synchronized with the motion stage is employed to enable or block the laser beam in specific regions during the fabrication process. The average energy per pulse impinging on the substrate can be tuned along the laser path rotating an halfwave plate placed next to a Glenn-Thomson polarizer. In addition, two flip mirrors allow to redirect the beam through a second harmonic generation stage in order to choose as processing laser wavelength the fundamental (at 1030 nm) or its half (at 515 nm).

3.1.1 THE LASER SOURCE

The laser source is a cavity-dumped mode-locker oscillator [76] developed in a collaboration between the Max Planck Institut of Heidelberg (Germany) and High-QLaser GmbH (Austria). The active medium is a $KY(WO_4)_2$ crystal, doped at 5 % concetration with Ytterbium. The laser emission wavelength is 1030 nm. The pumping system is based on a InGaAs multiemitter laser diode bar at 980 nm and the employed optical pump power is in the order of 15 W. The 8.9 m long cavity is wrapped in a footprint of 90 cm x 50 cm by a sequence of mirrors. The passive mode-locking regime is ensured by the utilization of a SESAM (SEmiconductor Saturable Absorbing Mirror) as the end mirror of the cavity and it allows to achieve a mode-locking pulse train at 17 MHz. Cavity dumping of the laser pulses is performed through the combination of a Pockels cell and a thin film polarizer. An external electronic driver is synchronized to the mode-locking pulse train and acts on the Pockels cell with adjustable voltage and repetition rate. The polarization rotation induced by the Pockels cell makes a part of the pulse energy to be reflected by the thin film polarized and be extracted from the cavity. The repetition rate of the laser system can be tuned from few KHz to 1.1 MHz, spanning the integer submultiples of 17 MHz. Acting on the pump power and the dumping ratio it is possible to adjust the pulse energy (up to 1 μJ) and the pulse duration (from about

250 fs to about 400 fs) according to the pseudo-solitonic regime sustained by the cavity [77].

3.1.2 THE MOTION STAGE

Aerotech 3D FIBERGlide three-axis motion stage provides the relative movement between the laser focal spot and the sample. Due to the combination of air-bearing and brushless linear electric motor, an arbitrary 3D path with high accuracy and smoothness in a volume of 100 x 150 x 5 mm^3 is achievable. Optical encoders to 1 nm resolution constantly monitor the stages position and allow an active control of the motion with errors below 100 nm. The system is computer controlled and is programmable by G-Code language (typically used in CNC machining) to perform the designed microfabrication.

3.2 CHARACTERIZATION SETUP

In this paragraph a brief introduction to the characterization measurements required to test the proper device functions and the relative instrumentation adopted is provided.

3.2.1 OPTICAL MICROSCOPE

The first evaluation of the fabricated devices is performed through an optical microscope. From the top surface observation it is possible to verify the uniformity of the waveguides and to check if errors occurred during the fabrication process in terms of interruptions or defects in their paths. Side view of the sample allows to analyze the cross-section of the waveguides and infer qualitative information on the fabrication process. To this target a Nikon ME600 microscope was used, equipped with an optional Differential Interference Contrast (DIC) module, which enables enhanced vision of small index contrasts by exploiting interference phenomena. A high resolution CCD Camera (PixeLINK B871) is mounted
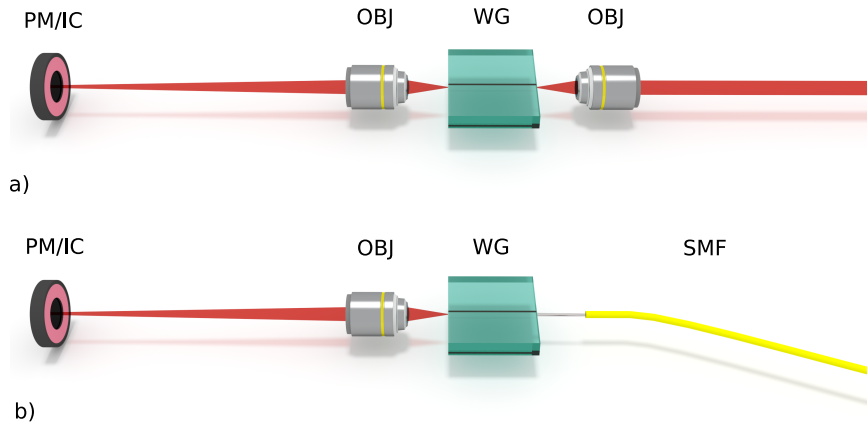
Figure 3.2.1: (a) End-fire coupling configuration for waveguide characterization. A microscope objective (OBJ) focuses the incoming laser beam into the waveguide (WG) input facet. Another microscope objective collects the output light and images it either on a power meter head (PM) or on an imaging camera (IC). b) Fiber-butt coupling. In this case, light is coupled to the device by directly facing the input facet to a single mode optical fiber (SMF). The image is taken from [75]

on the microscope for picture acquisition with a computer.

3.2.2 DEVICE COUPLING

The measurement of the radiation confinement properties of the waveguiding devices is one of the crucial step in their characterization. Light is coupled into the optical circuits as sketched in Fig.3.2.1. End-fire coupling configuration is represented in Fig. 3.2.1 a) and it consists in focusing a collimated laser beam to the input facet of the waveguide through a microscope objective or an aspheric lens. To achieve a good efficiency the beam waist at the focal point should match the mode radius and the numerical aperture NA of the employed objective should be comparable with the numerical aperture of the waveguide ($\sim$ 0.10 in femtosecond laser written waveguide). Another possible configuration is called "fiber-butt-coupling". The end of a single mode optical fiber (SMF) is cut, peeled and brought next to the input of the device. A stable and very precise alignment of the objective

43
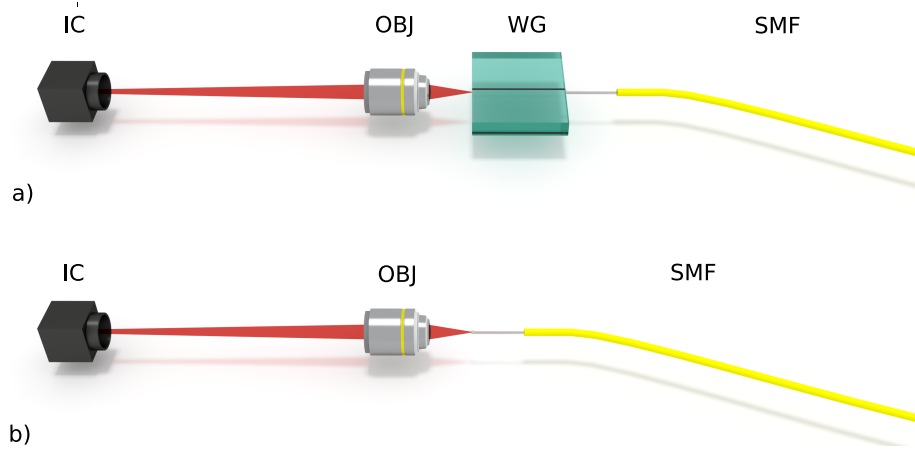
Figure 3.2.2: Schematic of the acquisition procedure of the spatial intensity profile of the mode supported by the waveguide, coupled with the fiber-butt configuration. First (a) the near field profile of the waveguide (WG) mode is measured with the imaging camera (IC). Then, (b) the chip is removed and the near field of the single mode fiber (SMF) mode is acquired for calibration. The image is taken from [75]

(or fiber) with the waveguide is necessary and so a sub-micrometric positioning system is employed. The objective (or the fiber) is therefore mounted on a manual three-axis micropositioner (NanoMAX, Melles Griot) with 50 nm resolution. The sample is hold by a four-axis manipulator (MBT402, Thorlabs). It allows two linear translation in the plane transverse to the optical axis and two tilt adjustments. In both configurations the output light is collected by another microscope objective with higher NA mounted on a three-axis stage manipulator and then imaged on a sensitive element (e.g a power meter head or a videocamera).

3.2.3 MODE PROFILE

The spatial intensity profile $I_{wg}(x,y)$ is one of the key property of the guided mode of a waveguide. How to measure it? First of all the waveguide is coupled employing the fiber-butt or the end-fire configuration and the near field profile of the output

mode is imaged on a high sensitivity vidicon camera (Hamamatsu C2400-03A). The whole visible range and the near infrared up to a wavelength of 1800 nm is covered by this camera. Paying specific attention to not saturating the dynamic response of the camera, the intensity profile is digitally acquired for the following elaboration. To calibrate the image dimension, the waveguide is removed and replaced by a fiber with a well-known (by producer specifications) mode diameter. The key step of this procedure is to keep the magnification ratio fixed in order to keep the distance between the collection objective and the input of the camera unchanged. A numerical analysis is performed on the acquired images, which allows to retrieve the mode intensity profile $I_{wg}(x,y)$. In the case of single mode waveguides, theory guarantees that its fundamental guided mode does not present sign inversion and so it is possible to calculate the spatial field distribution as:

$$\left| E(x, y) \right| = C \sqrt{I(x, y)}, \tag{3.1}$$

where C is a negligible constant, since the interesting element is the normalized profile. The overlap integral of the guided mode and the fiber mode profiles allows one to retrieve the coupling losses of the waveguides.

3.2.4   LOSSES MEASUREMENT

Insertion Losses (IL) are defined as the attenuation on the optical signal caused by the insertion of the sample and are one of the critical parameter in the characterization of an integrated optical device. They are typically expressed in decibels (dB) and they are represented as:

$$IL_{dB} = -10 \log_{10} \left(\frac{P_{out}}{P_{in}} \right), \tag{3.2}$$

where P_{in} and P_{out} are the optical powers at the input and output of the device. The IL can be directly calculated in fiber-butt configuration. First of all the power P_{out} is measured according to the scheme in Fig. 3.2.1 b). Then the sample is removed, the light coming from the fiber is collected by the same microscope objective and

it is sent to the power meter head in order to measure P_{in}. The measured values are now replaced in equation 3.2. IL can be decomposed in four different terms: Fresnel Losses (FL), Propagation Losses (PL), Coupling Losses (PL) and Bending Losses (BL).

- Fresnel Losses arise from the Fresnel reflections at the substrate-air interface induced by refractive index discontinuity. They can be represented by the following formula:

$$FL = -10 \log_{10} \left[1 - \frac{(n_2 - n_1)^2}{(n_2 + n_1)^2} \right], \qquad (3.3)$$

where n_1 and n_2 are the refractive indices of substrate and air respectively. In table 3.2.1 FL for the materials used in this thesis are listed. Obviously, in the calculation of total insertion losses, the written values must be doubled as FL occur at both sample facets. In the fiber-butt-coupling configuration FL can be made negligible applying index matching oil between the tip of the fiber and the input facet of the device.

- Coupling Losses derive from the mismatch between the electric field distribution $E_{in}(x,y)$ of the light impinging on the input facet of the device and the mode of the waveguide E_{wg}. It can be evaluated through the following formula:

$$CL_{dB} = -10 \cdot \log_{10} O, \qquad (3.4)$$

where O is the overlap integral:

$$O = \frac{|\iint E_{wg} E_{in} \, dx \, dy|^2}{\iint |E_{wg}|^2 \, dx \, dy \cdot \iint |E_{in}|^2 \, dx \, dy}, \qquad (3.5)$$

being E_{wg} and E_{in} numerically estimated using the method described in paragraph 3.2.3.

- Propagation Losses are caused by propagation of light inside a waveguide in

Table 3.2.1: Report on Fresnel Losses at the interface with air of the different substrates used in this thesis

n_1	n_2	FL[dB]	Element$_1$	Element$_2$
1.5	1	0.18	silicate glass	air
2.15	1	0.6	lithium niobate	air
2.15	1.5	0.14	lithium niobate	glass

the presence of roughness and non-homogeneity in its core refractive index profile. This deviation from perfect translational symmetry along the optical axis direction produces light scattering and coupling to radiative mode. The presence of centers of scattering and defects may also increase this term. An estimation of PL for a straight waveguide can be achieved indirectly by this equation:

$$PL_{\text{dB/cm}} = \frac{IL_{\text{dB}} - FL_{\text{dB}} - CL_{\text{dB}}}{l} \quad (3.6)$$

- Bending Losses originate from the distortion of the guided field distribution induced in the curved trajectory by a partial coupling to radiative modes. They increase exponentially by decreasing the radius R of curvature and are higher for waveguides with lower refractive index contrast due to their less confined guided mode. They can be estimated via the fabrication of a set of devices with different radii R_i and fixed bent path l_c through the next formula:

$$(BL_i)_{\text{dB/cm}} = \frac{(IL_i)_{\text{dB}} - (IL_{SWG})_{\text{dB}}}{l_c}, \quad (3.7)$$

where IL_i are the IL of the bent waveguides of radius R_i and IL_{SWG} are the IL of the straight waveguides.

47

Summarizing the above contributions, IL can be expressed through the following equation:

$$IL_{dB} = CL_{dB} + 2FL_{dB} + l \cdot PL_{dB/cm} + l_c \cdot BL_{dB/cm}, \qquad (3.8)$$

being l the total length of the waveguide and l_c the length of the curved section.

3.2.5 SHG Bandwidth

In order to evaluate the nonlinear properties of the fabricated waveguides with classical light, second harmonic generation measurements are performed. The output of a tunable laser (Agilent 8164B, maximum output power of 7 mW from 1440-1640 nm) is focalized into the realized waveguides through a 10x microscope objective in the end-fire coupling configuration. The polarization of the impinging light can be manipulated by the combination of a polarization controller (FPC561, Thorlabs) and a Glan-Thomson polarizer. The output of the waveguide is then collected by a 25X microscope objective and directed to a Silicon photodiode with a resposivity of 0.5 A/W and a gain of $1.1 \cdot 10^5$ V/W. The advantage of using a Si photodiode is its transparency to the pump wavelengths, which therefore doesn't perturb the second harmonic measurement. A scan of different pump wavelengths is automatically performed by the laser source and the response of the photodiode to the second harmonic is acquired through an oscilloscope. The laser system is directly connected with a channel of the oscilloscope, which acquires the trigger pulses emitted by the source at the start and the end of the sweep. A calibration between the time scale of the oscilloscope with the wavelength scale of the tunable laser can be performed. Thus the second harmonic profile as a function of the incident frequency and consequently the phase-matching bandwidth can be obtained. An estimation of the conversion efficiency can be performed acquiring the fundamental and SH powers through the Ge and Si heads of a powermeter (ML9001A, Anritsu). A sketch of the experimental setup is reported in Figure 3.2.3.
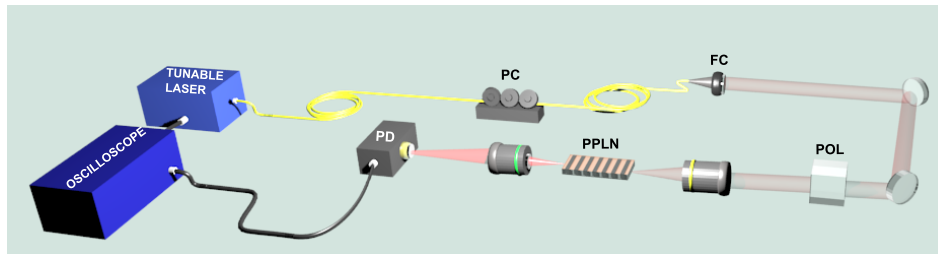
Figure 3.2.3: Schematic of the setup for the bandwidth characterization of the process of second harmonic generation. The output of a tunable laser is injected in the PPLN waveguides by means of a 10X microscope objective. A fiber collimator (FC) is employed to switch from fiber-butt-coupling configuration into the end-fire-coupling configuration in order to freely and completely manipulate the output polarization. In fact, the polarization of the impinging light is set to vertical by a Glan-Thomson polarizer (POL), while a polarizer controller (PC) is used to maximize its vertical component. The output light is collected by a 25X microscope objective and directed to a silicon photodiode. The laser source performs a frequency sweep and emits trigger pulses at the start and the end of the sweep. Both the output of the photodiode and the triggers are recorded by an oscilloscope leading to the acquisition of the bandwidth of the SHG process. The full control on the polarization is useful to maximize the signal to noise ratio of the bandwidth measurement and it is necessary to evaluate the conversion efficiency of the process.

4

On-chip photon-pair source

In Section 4.1 we briefly illustrate the motivation behind the project. A general description of the device is given in Section 4.2. The mathematical description of the components and the evolution of the state throughout them are explained in Section 4.3

4.1 MOTIVATION

The fabrication of fully integrated devices is an interesting prospect in quantum information. The possibility of miniaturization, scalability and stability offered by integrated optics should allow to realize high-complexity schemes, not achievable with previous setups. In this framework the fabrication of linear circuits is quite consolidated and has already led to the implementation on chip of single building blocks for quantum computing and simulation processes. In order to reach a conversion toward a fully integrated quantum platform, photon-number states sources and detectors must be developed and combined on chip. Concerning integrated sources, SPDC in periodically poled nonlinear waveguides represents a promising approach, due to its intrinsic advantages over bulk configuration (see paragraph 4.3.2).

4.2 GENERAL DESCRIPTION

In this thesis we will develop the optical components for the realization of an integrated photon-pair source at telecom wavelength based on a degenerate SPDC process in periodically-poled lithium niobate (PPLN) waveguides. The source will be composed of three cascaded integrated-optics devices (see Fig. 4.2.1), respectively fabricated in glass, PPLN and glass again through femtosecond laser writing. This hybrid approach is a promising route to exploit the specific advantages of each substrate and has emerged as a solution to the challenges of monolithic integration through the combination of components and techniques which are optimized for their individual function. In particular, high-quality and low-loss linear optical circuits can be realized in glass by means of FLM.
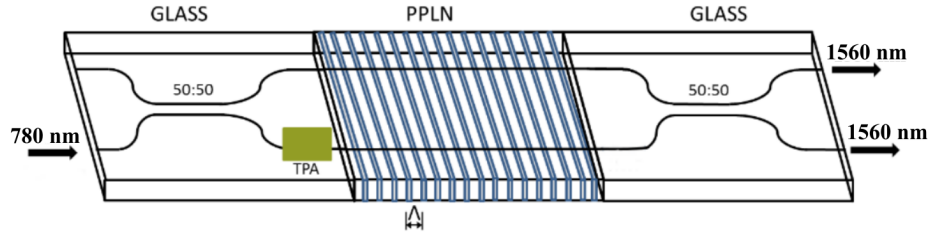
Figure 4.2.1: Schematic of the experimental chip for pair-photon generation. The pump light, impinging on an input port of a balanced directional coupler, is equally split and directly coupled to an array of two waveguides in PPLN. A pair of photons is thus generated in one of the two nonlinear waveguides through SPDC. The poling period Λ is designed to obtain degenerate down-conversion at 1560 nm. A path-entangled state is generated at the output of the II chip. By controlling phase by means of the thermal phase adjuster (TPA), it is possible to obtain a separated state: one photon at each of the two output ports of the balanced directional coupler in the third chip.

The pump laser light at 780 nm, linearly polarized, is injected in one input of the balanced directional coupler, which splits the pump into two distinct optical modes. A thermal phase adjuster is placed above one arm of the interferometer in order to control the phase shift $\Delta\Phi$ between the two paths. The second chip is composed by an array of two parallel straight waveguides in PPLN substrate. The poling period is selected to provide quasi-phase matching condition for type o SPDC process (the daughter photons share the same polarization $|V\rangle$ of the pump photon in a collinear geometry). By neglecting the probability that a photon-pair is generated in both waveguides simultaneously, a path-entangled state is generated at the output of the second device:

$$|\Psi\rangle_{PPLN} = \frac{|0,2\rangle + e^{i\Delta\varphi}|2,0\rangle}{\sqrt{2}}, \tag{4.1}$$

where the relative phase $\Delta\varphi$ is transferred from the intrinsic phase difference of the pump modes at the input of the second chip. This phase bias can be addressed to:

- Small variations in the fabrication parameters during the inscription of the two arms of the directional coupler, which may induce slightly different re-

fractive index changes.

- A misalignment in the coupling between each output arm of the directional coupler with the corresponding nonlinear waveguide.

The third chip consists in a balanced directional coupler at 1560 nm and, in the case of $\Delta\varphi = 0$, it works as a time-reversed Hong-Ou-Mandel interferometer realizing a deterministic separation of the indistinguishable entangled photon pair (i.e. the twin photons generated in one PPLN waveguide are always emitted one from each arm of the final directional coupler). In the general case an intrinsic phase difference $\Delta\varphi$ is present between the paths, therefore the additional controllable phase induced by the thermal phase adjuster is required to obtain the following state:

$$|\Psi\rangle_{out} = \underbrace{\frac{|0, 2\rangle - |2, 0\rangle}{\sqrt{2}}}_{|\Psi_{Bunch}\rangle} \cos\left(\Delta\Phi'/2\right) + \underbrace{|1, 1\rangle}_{|\Psi_{Sep}\rangle} \sin\left(\Delta\Phi'/2\right), \qquad (4.2)$$

where $\Delta\Phi' = \Delta\Phi + \Delta\varphi$.

The output state is thus a superposition of the two-single-photon state $|\Psi_{Sep}\rangle$ when $\Delta\Phi' = 2\pi n$ with $n \in \mathbb{N}$ and the bunched state $|\Psi_{Bunch}\rangle$ when $\Delta\Phi' = \pi(2n + 1)$.

4.3 MATHEMATICAL DESCRIPTION

In order to describe the evolution of the input state due to its propagation through the device, the unitary transformations associated with each optical element is shown below. A great attention is reserved to SPDC waveguides.

4.3.1 DIRECTIONAL COUPLER AND PHASE SHIFTER

A directional coupler represents the integrated optics version of the bulk beam splitter. It is a four-ports component and its typical design is represented in Figure 4.3.1. Two parallel and not interacting straight waveguides are brought close

together achieving a light transfer by evanescent field coupling. The waveguides are then decoupled restoring the initial distance at the output of the device. The splitting ratio of the directional coupler can be set by the proper engineering of the interaction length L and the distance coupling d.
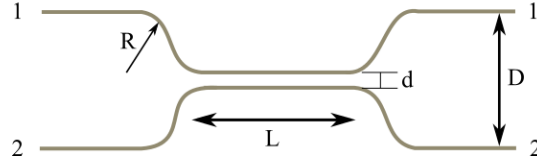
Figure 4.3.1: Schematic of the structure of the directional coupler. Two decoupled waveguides at distance D are brought close through an S-bend of radius R. They interact in a region of length L and distance d by means of evanescent field coupling.

The reflectivity and the transmission of the directional coupler can be defined in the following way:

$$
R = \frac{P_{out1}}{P_{in1}}
$$
$$
T = \frac{P_{out2}}{P_{in1}}
$$

(4.3)

The field transfer matrix U_{DC} of a loss-less directional coupler can be represented as:

$$
\begin{bmatrix} E_{out1} \\ E_{out2} \end{bmatrix} = \begin{bmatrix} \sqrt{R} & i\sqrt{T} \\ i\sqrt{T} & \sqrt{R} \end{bmatrix} \begin{bmatrix} E_{in1} \\ E_{in2} \end{bmatrix},
$$

where R and T are the reflectivity and the transmission of the device. In the case of a balanced directional coupler $R = T = 1/2$.

In the quantum framework, the following matrix equation holds for the annihilation operators:

$$
\begin{bmatrix} \hat{a}_{out1} \\ \hat{a}_{out2} \end{bmatrix} = \frac{1}{\sqrt{2}} \begin{bmatrix} 1 & i \\ i & 1 \end{bmatrix} \begin{bmatrix} \hat{a}_{in1} \\ \hat{a}_{in2} \end{bmatrix}
$$

(4.4)

The matrix equation of a phase shifter φ acting on output mode 1 of the direction

coupler above can be expressed as:

$$\begin{bmatrix} \hat{a}_{out1} \\ \hat{a}_{out2} \end{bmatrix} = \frac{1}{\sqrt{2}} \begin{bmatrix} e^{i\varphi} & 0 \\ 0 & 1 \end{bmatrix} \begin{bmatrix} \hat{a}_{out1} \\ \hat{a}_{out2} \end{bmatrix} \tag{4.5}$$

4.3.2 SPONTANEOUS PARAMETRIC DOWN CONVERSION

Starting from the classical electric field energy density for a non-linear non-centrosymmetric medium and quantizing the electric field, it is possible to obtain a quantum mechanical description of the process:

$$\hat{H}_{SPDC} = \varepsilon_0 \iiint \chi_2 \hat{E}_p^{(+)} \hat{E}_s^{(-)} \hat{E}_i^{(-)} \, d^3r + \text{H.c.}, \tag{4.6}$$

where χ_2 is the nonlinear susceptibility, ε_0 the vacuum permittivity and $\{p, s, i\}$ stands for the pump, the signal and the idler, respectively. The Hermitian conjugate represents the second harmonic generation process. High-order nonlinearities will be neglected in this analysis.

Considering a relatively intense incoming pump field, the weakness of the non-linear interaction allows to neglect pump depletion and treat it as a classical field:

$$E_p^{(+)} = \int dw_p a(w_p) \, e^{i(\vec{k}_p(w_p) \cdot \vec{r} - w_p t)}, \tag{4.7}$$

where the function $a(w_p)$ represents the spectrum and the amplitude of the pump field. Hereinafter, we will assume that the pump field is produced by a continuous wave laser source with central frequency w_c and thus $a(w_p) = E_p \, \delta(w_p - w_c)$.

The idler and the signal fields will be instead represented in the canonical quantization formalism as they describe single-photon fields.

$$E_j^{(-)} = -i \sum_k \sqrt{\frac{\hbar w_{k,j}}{2\varepsilon_0 V}} \vec{\varepsilon}_k \hat{a}_{k,j}^\dagger e^{-i(\vec{k}_j \cdot \vec{r} - w_{k,j} t)}, \tag{4.8}$$

being $j = \{s, i\}$.

We investigate the case of collinear propagation along the z-axis of the crystal,

neglecting the transverse degrees of freedom. We further restrict the analysis to single mode emission from signal and idler fields discarding the sum over k. With these hypothesis Equations 4.7 and 4.8 become:

$$E_p^{(+)} = E_p\, e^{i(k_p z - w_p t)}$$

$$\hat{E}_j^{(-)} = -i\sqrt{\frac{\hbar w_j}{2\varepsilon_0 V}}\,\hat{a}_j^\dagger\, e^{-i(k_j z - w_j t)}$$

$$(4.9)$$

In the Schrodinger picture, the quantum state evolution for SPDC is given by:

$$|\psi(t)\rangle = \exp\left[\frac{1}{i\hbar}\int_0^t \hat{H}_{SPDC}(t')\,dt'\right]|o\rangle \tag{4.10}$$

The first-order perturbation expansion leads to:

$$|\psi(t)\rangle = |o\rangle + \frac{1}{i\hbar}\int_0^t \hat{H}_{SPDC}(t')\,dt'\,|o\rangle, \tag{4.11}$$

where the zero-order term represents vacuum emission, the first-order term represents photon-pair emission and high-order photon-pairs emission can be neglected as long as the pump field is not too bright. Combining equations 4.6, 4.9 and 4.10, we arrive at:

$$\int_0^t \hat{H}_{SPDC}(t')\,dt' = A\,E_p \int_0^t dt'\, e^{-i(w_p - w_i - w_s)t'} \int_0^{L_z} dz \chi_2(z)\hat{a}_s^\dagger \hat{a}_i^\dagger e^{i(k_p - k_i - k_s)z} + H.c,$$

$$(4.12)$$

where all constants are gathered in A. Performing the temporal and the spatial integration with the assumption that $\chi_2(z) = \chi_2$, we obtain:

$$\int_0^t \hat{H}_{SPDC}(t')\,dt' = A\,E_p \chi_2\, e^{-\frac{i\Delta wt}{2}}\, e^{\frac{i\Delta k L_z}{2}}\, t\, sinc\left(\frac{\Delta wt}{2}\right) L_z sinc\left(\frac{\Delta kz}{2}\right) \hat{a}_s^\dagger\, \hat{a}_i^\dagger + H.c,$$

$$(4.13)$$

where $\Delta k = k_p - k_s - k_i$ and $\Delta w = w_p - w_s - w_i$.

If the interaction time t is long enough, the temporal sinc function can be ap-

proximated with a delta leading to the following output state:

$$|\psi(t)\rangle = |0\rangle + A\,E_p\chi_2\,e^{-\frac{i\Delta wt}{2}}\,e^{\frac{i\Delta kL_z}{2}}\,\delta\!\left(\frac{\Delta w}{2}\right)L_z sinc\!\left(\frac{\Delta kz}{2}\right)\hat{a}_s^\dagger\,\hat{a}_i^\dagger\,|0\rangle \qquad (4.14)$$

As described in the above equation, signal and idler are always produced in pair. An efficient production of photon pair requires that:

$$\begin{aligned} w_p &= w_s + w_i \\ k_p &= k_s + k_i, \end{aligned} \qquad (4.15)$$

which are the energy conservation and phase-matching conditions.

QUASI PHASE MATCHING

As stated in 1.2.3.1, the wave-vector conservation is usually achieved through bire-fringent phase-matching or quasi-phase-matching. In our device the latter con-figuration is employed and the subsequent modification on the Hamiltonian will be discussed below. In birefringent phase-matching the chromatic dispersion is made negligible exploiting anisotropy of the crystal, while in QPM the interact-ing fields still propagate with different phase velocities. When the accumulated phase mismatch reaches π, the sign of the nonlinear susceptibility is reversed. At this point destructive interference between the fields, that would happen in the phase-mismatched configuration, is avoided by setting their phase difference to zero. The phase difference then increases again, as the fields propagate, until it reaches π again, when the nonlinear susceptibility is reversed once more. There-fore the output power grows along the crystal length as represented in Fig. 4.3.2.

In ferroelectric crystals the sign of the nonlinear coefficient is modulated through a periodically inversion of the spontaneous polarization P_S. As a consequence, a spatial dependence of the effective nonlinear coefficient is introduced according to:

$$\chi^{(2)}(z) = \chi_o^{(2)}\,sign\!\left(\cos\frac{2\pi z}{\Lambda}\right) \qquad (4.16)$$
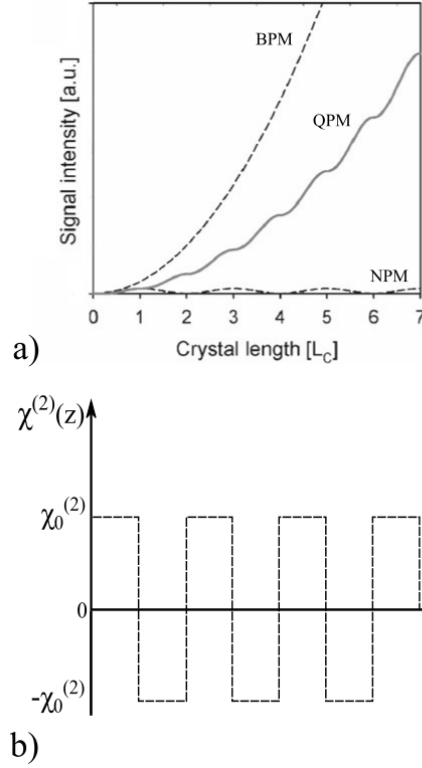
Figure 4.3.2: In figure (a) the signal intensity growth is represented as a function of the coherence length L_C for the birefringent phase-matching (BPM), the quasi-phase-matching (QPM) and the phase-mismatched (NPM) cases. In figure (b) the modulation of the nonlinear coefficient with a period Λ is schematically drawn for the first-order (m=1) configuration.

In the Fourier domain it can be represented as:

$$\chi^{(2)}(z) = \sum_{m=-\infty}^{+\infty} G_m e^{ik_m z}, \qquad (4.17)$$

where

$$k_m = \frac{2\pi m}{\Lambda}$$

$$G_m = \frac{1}{\Lambda} \int_{-\Lambda/2}^{+\Lambda/2} \chi^{(2)}(z) e^{-ik_m z} dz, \qquad (4.18)$$

59

Replacing Eqn. 4.16 in the integral above, we obtain:

$$G_m = \frac{1}{\Lambda} \int_{-\Lambda/2}^{+\Lambda/2} \chi_o^{(2)} \underbrace{sign\left(\cos\frac{2\pi z}{\Lambda}\right)}_{even\ function} e^{-ik_m z} dz = \frac{2\chi_o^{(2)}}{\pi m} \sin\left(\frac{m\pi}{2}\right) \quad (4.19)$$

The nonlinear coefficient can thus be represented as:

$$\chi^{(2)}(z) = \sum_m \frac{2\chi_o^{(2)}}{\pi m} \sin\left(\frac{m\pi}{2}\right) e^{-\frac{2\pi m}{\Lambda}} \quad (4.20)$$

The maximum value of the above function is obtained when $|m| = 1$ and therefore the most efficient configuration is the one with an inversion of nonlinear coefficient every interaction length. Replacing the z-dependent $\chi^{(2)}$ in equation 4.12 leads to:

$$\int_0^t \hat{H}_{SPDC}(t')\,dt' = \frac{2A}{\pi}E_p\int_0^t dt' e^{-i(w_p-w_i-w_s)t'}\int_0^{L_z} dz\chi_o^{(2)}\hat{a}_s^\dagger\hat{a}_i^\dagger e^{i(k_p-k_s-k_i-\frac{2\pi}{\Lambda})z} + h.c,$$

$$(4.21)$$

The integration of the above equation will lead to a formally identical solution as in the case of constant nonlinear coefficient. The key difference, apart from the factor $2/\pi$, consists in the additional term in the phase-matching condition:

$$k_p = k_s + k_i \rightarrow k_p = k_s + k_i + \frac{2\pi}{\Lambda} \quad (4.22)$$

The new degree of freedom Λ brings the following benefits:

- The proper design of the poling period Λ allows to freely choose the wavelength of the daughter photons.

- For fixed choice of photon-pair wavelength, the propagation direction of the generated pairs can be made collinear with the pump photons, eliminating spatial walk-off effects in the transverse direction. In the absence of walk-

off, the effective interaction length inside the medium increases leading to an enhanced conversion efficiency.

- The polarization of the three interacting fields can be arbitrary chosen allowing to use the largest component of the nonlinear susceptibility tensor and maximize conversion efficiency in a given nonlinear medium.

- Exploiting the temperature dependence of the refractive index and of the poling period (due to the thermal expansion of the medium), the idler and signal wavelengths can be controlled of several nm by varying the temperature of the device.

- Non-periodic modulation of the nonlinear coefficient allows to achieve complex phase-matching conditions.

Waveguided SPDC

Actually our nonlinear chip relies on waveguided SPDC process. The main difference of waveguided parametric down-conversion with respect to the bulk model is the dependence of the output state on the overlap integral over the three interacting spatial field distributions, $f(x, y)$, propagating along the waveguide.

$$O_{klm} = \iint dx\, dy\, f_p^{(k)}(x, y) f_s^{(l)}(x, y) f_i^{(m)}(x, y) \qquad (4.23)$$

The efficiency of the down-conversion is thus dependent on the spatial-mode of the three interacting fields. When pump, idler and signal propagate in similar modes, the output will be generated with high efficiency. Furthermore, the phase-matching function is also dependent on the spatial-mode triplet. In fact, different spatial modes lead to a modification of the effective propagation constant β resulting in the translation of the phase-matching function in the frequency space.

Despite a weak increase in loss rate due to an additional loss contribution by means of scattering in the waveguiding structure, the PDC process in waveguides presents several advantages over bulk-PDC sources.

- The engineerization of the waveguiding structure allows to control the generated spatial distributions. In fact, photon-pairs emitted in bulk SPDC are spread into a large set of spatial modes at different angles, while waveguided photon-pairs are emitted in well-defined spatial modes in order to achieve high collection efficiency and coupling into optical fibers.

- The confinement of SPDC inside a waveguide leads to an increased overlap of the involved fields O_{klm} and to the restriction of the interaction couplings to a discrete number of modes. The photon-pair generation probability is thus enhanced.

- The interaction of the three fields is strictly collinear simplifying experimental alignment and post-processing operations.

Neglecting the multiple-pairs emission, the Hamiltonian for waveguided SPDC will be approximated in the next calculation as follows:

$$\hat{H}_{SPDC} \propto \hat{a}_p \, \hat{a}_s^\dagger \, \hat{a}_i^\dagger \tag{4.24}$$

4.3.3 STATE EVOLUTION

The following description is based on the device layout represented in Fig. 4.2.1.

The initial state impinging on the first chip is :

$$|\psi\rangle_{in} = |1\rangle_1 \, |0\rangle_2 \,, \tag{4.25}$$

where a photon is injected in input 1 of the directional coupler and no photons are injected in the second input arm.

Being the first device composed by a cascade of a balanced directional coupler and a phase shifter, its overall matrix T_{FD} can be described as follows:

$$T_{FD} = T_{\Delta Phi} \cdot T_{DC_1} = \begin{bmatrix} e^{i\Delta\Phi} & 0 \\ 0 & 1 \end{bmatrix} \cdot \frac{1}{\sqrt{2}} \begin{bmatrix} 1 & i \\ i & 1 \end{bmatrix} = \frac{1}{\sqrt{2}} \begin{bmatrix} e^{i\Delta\Phi} & i\,e^{i\Delta\Phi} \\ i & 1 \end{bmatrix} \tag{4.26}$$

At the output of the first chip the state becomes:

$$|\psi\rangle_{chip1} = T_{FD} \cdot |\psi\rangle_{in} = \frac{1}{\sqrt{2}} \left[e^{i\Delta\Phi} |1\rangle_3 |0\rangle_4 + i |0\rangle_3 |1\rangle_4 \right]. \qquad (4.27)$$

The state now propagates into the nonlinear waveguides, which in our application can be represented by the not normalized Hamiltonian in the equation 4.24. Therefore the output state is:

$$|\psi\rangle_{chip2} \xrightarrow{\hat{a}_p \hat{a}_s^\dagger \hat{a}_i^\dagger} \frac{1}{\sqrt{2}} \left[e^{i\Delta\Phi} |2\rangle_A |0\rangle_B + i |0\rangle_A |2\rangle_B \right]. \qquad (4.28)$$

A path-entangled state is obtained: twin-photons are generated in the A or the B waveguide. The interaction between the $|\psi\rangle_{chip2}$ and the second balanced directional coupler results in the following state:

$$|\psi\rangle_{out} = T_{DC2} \cdot |\psi\rangle_{chip2} = \underbrace{\frac{|0,2\rangle - |2,0\rangle}{\sqrt{2}}}_{|\Psi_{Bunch}\rangle} \cos\left(\Delta\Phi/2\right) + \underbrace{|1,1\rangle}_{|\Psi_{Sep}\rangle} \sin\left(\Delta\Phi/2\right) \quad (4.29)$$

Since we are interested in the generation of a pair of indistinguishable photons, which is represented by state $|\Psi_{Sep}\rangle$, the thermal phase adjuster should be employed to drop to zero the probability of the bunched state $|\Psi_{Bunch}\rangle$.

In the above mathematical description we have made the following assumptions:

- A single photon state was chosen as input state in order to make the calculation easier. In the experiment a coherent state will be injected in an input port of the directional coupler. The balanced directional coupler will equally split the power between its two output arms and therefore nonlinear waveguides will be simultaneously excited. Since the nonlinear SPDC process occurs with low probability, the probability that both waveguides will generate a photon-pair at the same time is negligible. Considering a coherent state as input and neglecting the probability that a photon-pair is

generated in both the waveguides simultaneously, the same output state of equation 4.29 is in any case obtained.

- In the Hamiltonian of the SPDC process we have neglected high order generation terms. In order to limit the contribution of multiple-pairs emission, the injected power should be limited.

5

Manipulation and Routing

This chapter deals with the fabrication and the characterization of the linear integrated glass devices depicted in figure 4.2.1. In section 5.1 the realization of a balanced directional coupler at 780 nm with a thermal phase modulator is discussed. The 2π control of the relative phase between the DC arms with low dissipation power is the main requirement of this chip. In section 5.2 we deal with the fabrication of a balanced directional coupler at 1560 nm. It has to be composed by symmetric waveguides and to present low insertion losses. Both devices have to fit in a short length and to couple well with the intermediate nonlinear chip.

5.1 Balanced directional coupler and thermal heater

5.1.1 Preliminary fabrication

As stated in section 2.2, FLM technique depends on several fabrication parameters, which should be optimized according to the requirement of each application. Aiming to find the optimum parameters for the realization of a balanced directional coupler (DC) at an operating wavelength of 780 nm, several straight waveguides were fabricated with different irradiation parameters. Since the space of parameters to be optimized has very large dimensions, we limited the analysis to pulse energy and relative translation speed, while setting all the other parameters to literature indication and previous experience on the selected substrate. In section 5.1.1.1 the design of the DC is presented. It was realized taking into account the subsequent fabrication of resistive heaters, whose design and characterization are shown in section 5.1.2.

5.1.1.1 Fabrication parameters and geometry

The waveguides were realized in Aluminum-Borosilicate glass (Eagle2000, Corning Inc.) through the fabrication setup that was introduced in Figure 3.1.1. The femtosecond pulses, produced by the Yb:KYW cavity dumped laser system, were focused inside the substrate by a 50x (NA 0.6) objective. The repetition rate of the laser system was fixed at 1 MHz according to previous optimization for this material. The transverse writing geometry was employed in order to exploit the advantages of this configuration, which were presented in paragraph 2.2.2.

In the definition of the inscription depth we had to take into account the following trade-off:

- The sensibility of the fabrication process to surface roughness and material stress near the surface is higher for the inscription of shallow structure and

66

Fabrication parameters	
Laser system	Yb:KYW cav. dump.
Wavelength	1030 nm
Repetition rate	1 MHz
Pulse energy	220 nJ
Translation speed	40 mm/s
Objective	0.6 NA

Table 5.1.1: Waveguide writing parameters used for realizing the balanced directional coupler at 780 nm.

this may give rise to additional propagation losses.

- The deeper the directional coupler is fabricated, the higher should be the power dissipated on the resistive heater to induce the desired phase modulation leading to an increase of the amount of heat which will diffuse in the glass. Even if the induced temperature variations will not represent a problem in the functioning of the directional coupler and in its alignment with the input optical fibers and the PPLN crystal, part of the accumulated heat could diffuse in the connected second device leading to an unpredictable local variation of the phase-matching function and thus of the emitted spectrum.

Since temperature stability of the photon source is a thorny problem and small variations should be compensated in order to stabilize the wavelength of the emitted photons, the maximization of the thermo-effect represents the more pressing requirement in the choice of inscription depth allowing to minimize the impact of heat diffusion on the nonlinear waveguides and to impose a $[0, 2\pi]$ phase shift between the two arms of the directional coupler. As stated above, the thermo-optical modulation of the phase should be performed without an excessive power dissipation in the resistive heaters, which could lead to a temperature increase of the substrate or, in the worst case, to the damage of the device. The phase delays accumulated in the two arms of a directional coupler under the action of the thermal phase adjuster is given by $\Phi = a\,P$, where P is the power dissipated in

the resistive heater and a is a geometry dependent parameter. Considering a wire-like heater configuration and neglecting the heat dissipation into air, Flamini et al. [78] proposed an analytic expression for a, given the distances ρ_1 and ρ_2 of the two interferometer's arm from the heater:

$$a = \frac{2n_T}{\lambda} \frac{1}{k} \frac{L_{arm}}{L_{wire}} \ln \frac{\rho_1}{\rho_2}, \qquad (5.1)$$

where $n_T = 1 \cdot 10^{-5} \text{ K}^{-1}$ is the thermo-optic coefficient, $\lambda = 780$ nm is the wavelength, $k = 0.9 \text{ W m}^{-1} \text{ K}^{-1}$ is the thermo-optical conductivity of the substrate, L_{arm} is the length of the straight segments in the interferometer's arms and L_{wire} is the length of the wire-like resistor. It can be straightforwardly retrieved from the model that shallow structures will present an higher value of a. All things considered, an inscription depth of 25 μm represents a good trade-off between the highest thermo-optic modulation and acceptable losses. Furthermore, an high value of a allows to obtain the 2π phase shift without the need of excessive device lengths and leads to the realization of more compact structures.

Analysis on insertion losses of several straight waveguides machined with different combinations of pulse energies (from 190 nJ to 280 nJ with step of 10 nJ) and inscription speeds (10-20-40 mm/s) was performed leading to the definition of optimum fabrication parameters, which are reported in Table 5.1.1.

In the design of the planar directional coupler we had to take into account the successive processes, which would be necessary for the realization of resistors on the surface of the substrate. According to the model proposed by Flamini et al. [78], the wire-like configuration was chosen for the thermal phase shifter. To maximize the region involved in the thermo-optic modulation, a directional coupler with long output straight arms, on which the resistors would be placed in the subsequent step, is designed. The radius of curvature was set at 60 mm by a trade-off between bending losses and the total bend lengths. The horizontal distance between the two arms of the directional coupler was set at 127 μm in order to match the standard distance between the outputs of fiber arrays, which will be used to inject light in the final experiment. The definitive design of the balanced directional
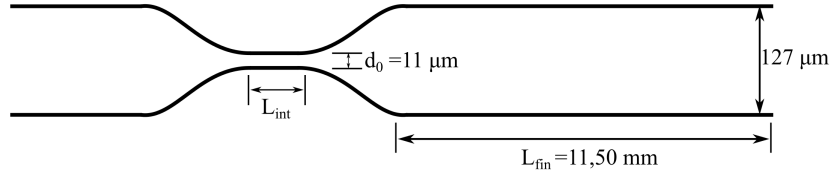
Figure 5.1.1: Schematic of the directional coupler with a fixed length $L_{fin} =$ 11.5 mm to allow the subsequent patterning of thermal shifters.

coupler is sketched in Figure 5.1.1.

We performed a length-scan approach in order to find the coupling length L_{3dB} and compensate process variability: several directional couplers were fabricated and each of them differs from the others by small interaction length variation. Applying this procedure allows us to translate any process tolerances in the variation of the L_{3dB} from the expected one. In table 5.1.2 the best couplers are reported. The wire-like heaters were placed on these devices, even if not all of them were perfectly balanced. This choice was made in order to have a back-up solution in the case of unbalanced generation by the two nonlinear waveguides in the SPDC process. In fact, process variability during waveguide inscription in the crystal can lead to the fabrication of slightly different waveguides in terms of losses, of guided modes at fundamental and down-converted wavelengths and of nonlinear properties: i.e. the femtosecond laser - crystal interaction can partially, or even completely, disrupt the nonlinear coefficient of the medium (see 2.3.2). The effect of not identical losses and effective nonlinear coefficients on the generation process is intuitive, while the role of guided modes should be clarified. As stated in paragraph 4.3.2, the efficiency of the waveguided SPDC process depends on the overlap integral O over the guided modes of the three interacting fields along the waveguide. Therefore, an inequality of this term between the two waveguides will reflect on a different generation efficiency and a different spectrum of the source (the phase-matching function is also dependent on the spatial-mode triplet). In addition, the overlap integral over the excitation mode of the directional coupler and the ex-

Chosen BS devices		
Device number	Interaction Length	Splitting Ratio
1	500 μm	50.6/49.4
2	700 μm	48.3/51.7
3	900 μm	43.4/56.6
4	1100 μm	37.2/62.8

Table 5.1.2: The splitting ratio of the four DC devices that showed the best performance, out from the 12 devices that were fabricated in a length scan approach.

cited mode of the nonlinear waveguide defines the coupling losses between the two cascaded devices. Therefore, different overlap integrals lead to different coupling losses and thus an unbalanced pumping of the array even with an ideal 3 dB directional coupler. A possible strategy to deal with the problem of unbalanced generation is represented by the excitation of the two nonlinear waveguides with a different mean number of photons, which should allow to equalize the generation rate at the two output ports and obtain the path-entangled state in equation 4.1. Since an active control of the splitting ratio of the directional coupler cannot be achieved with this configuration (the heaters allow only to manipulate the relative phase between the two output arms of the directional coupler), we decided to adopt a static strategy selecting a set of directional couplers with different splitting ratio.

5.1.2 Thermal shifter: design and characterization

After the characterization and the choice of the passive devices, we added thermal shifters on them realizing metallic resistors on the sample surface. The local temperature increase induced by the heaters on the coupler's arms allows to modulate the refractive index of the buried waveguides, leading to the accumulation of a relative phase between the arms of the directional coupler.

5.1.2.1 Design and Fabrication

In the design of the resistor we had to take into account the following requirements:

- the power has to be primary dissipated on the device's arms in order to induce a local modulation of the refractive index. This means that the heaters have to present a big resistance respect than the other electric components.

- the power per unit of area has to be acceptable in order to avoid the damage of the electrodes.

To fulfill the previous requirements long and narrow rectangular resistors were designed.

The pattern of the thermal heaters was realized through laser ablation of the 50 nm gold layer, deposited on the substrate surface by means of a sputter coater (Cressington, 108auto), employing the same femtosecond laser used for waveguide inscription. Since the coating procedure requires the detachment of the sample from the translation stage of the laser system in Fig.3.1.1, alignment markers were machined on the glass surface just after the fabrication of the directional couplers. The markers were made up of laser ablated straight grooves, sufficiently deep to be still visible after the deposition of the gold layer. Exploiting these ablation lines, it was possible to align the frame of reference of the previously fabricated directional couplers with the one of the phase shifters. The observation of the reference markers was performed focalizing on the sample surface the attenuated (in order to not damage the thin gold layer) laser beam and collecting the back-reflected light with a CCD. In the alignment process the second harmonic of the laser system in Fig.3.1.1 was employed, since it presents a smaller spot size and allows to distinguish smaller features. As a consequence, the same laser beam was used for the definition of the resistors. The ablation of the heaters pattern was machined using a translation speed of 1 mm/s and a pulse energy of 80 nJ. In order to guarantee a better electrical isolation between contacts, each isolating line was

fabricated by nine successive ablation lines with an offset of 500 nm, achieving an overall groove width of $\sim 5\ \mu m$.

A top-view schematic of the heater design is shown in Figure 5.1.2 (a). The black lines represent the directional coupler realized at 25 μm beneath the surface. The yellow zone represents the deposited gold layer. The white lines represent the ablation lines, which define the rectangular resistor and the larger regions employed to facilitate the electric connections. In Figure 5.1.2 (b), the top-view schematic of the whole chip is represented. As in the panel (a) of Figure 5.1.2, light blue colour is employed to underline the isolated region between the wires. The contacts were realized by bonding copper wires with an electrically conductive polymeric paste on the six rectangular pads (the common electrode presents a back-up bonding). The black dashed circles represent the position of the wires on the gold surface. The whole surface was then covered with an UV glue in order to protect the fragile gold layer and the bonds from possible damage or interruption. As indicated in zoom window of Figure 5.1.2 (b), the thermal phase modulators were not directly placed on the directional couplers' arms: the center of the rectangular resistor is shifted of 64 μm with respect to the position of the straight segment of the directional coupler. Exploiting this configuration, the 127 μm wide resistors allow to symmetrically induce phase modulation both on the lower arm of the upper directional coupler and on the upper arm of the lower one. Resistors R_{BE}, R_{CE} and R_{GE} are shared by two different devices.

5.1.2.2 CHARACTERIZATION

The phase difference induced by each resistor was characterized by a Young interferometer experiment: i.e. the two slits of the original experiment are replaced by the two outputs of the directional coupler, which are separated by 127 μm. The heaters were connected to a stabilized power supply (HQ power PS23023), which allowed to control the driving voltage between the two electrodes. In order to perform a full characterization of the thermo-optic effect as a function of the dissi-
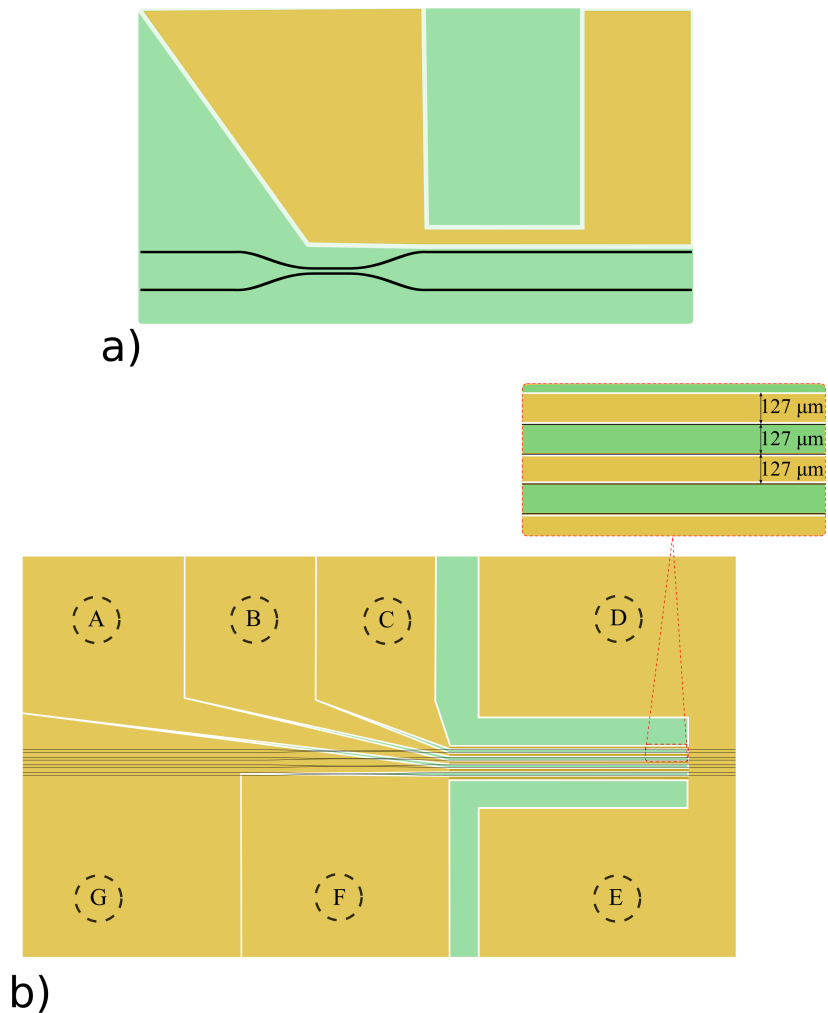
a)

127 μm
127 μm
127 μm

b)

Figure 5.1.2: (a) Top-view schematic of a region of the glass with the fabricated DC. The black lines represent the directional coupler, which is 25 μm under the surface. The 50 nm sputtered gold layer is represented by the yellow colour. The white lines represent the ablation pattern, which drives the 8 mm long resistor, that work as thermal shifters, and two electrical pads. (b) Overall design of the device. The glass footprint is 1.3 x 2.4 cm². The map colour is the same of the one in panel (a). The light blue regions are sketched in order to make the identification of the five wires and the isolated regions easier. The black circles present the location of the electric copper wire on the electrical pads (D and E represent the same electrode, which has a double connection). In the inset the geometry of wires is made evident. The heater is placed between two different directional coupler and presents a width of 127 μm to symmetrically control both devices.
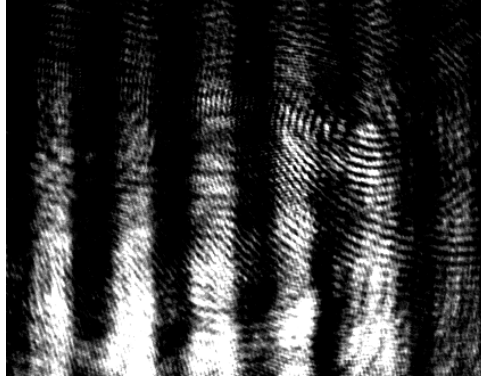
Figure 5.1.3: Interference pattern in a Young interference experiment acquired by the CCD camera with a driving voltage of 0 V. Varying the voltage across the resistor allows to retrieve the induced phase difference at the BS output.

pated power, the far-field interference profile was acquired with a CCD camera and an analysis was performed on the profile after its acquisition. A Fast Fourier Transform algorithm was applied on the profile in order to retrieve the relative phase between successive images, which differ one from the other in the applied voltage on the resistor. An example of such interference profile is reported in Figure 5.1.3.

Talking about an ohmic resistive heater, the driving voltage can be directly related to the dissipated power by the Joule law: $P = \Delta V^2/R$. In Figure 5.1.4 the experimental data for both arms of the first device are reported. Applying voltage on upper or lower arm of the directional coupler allows to induce a relative phase modulation in opposite directions. Therefore the design presents two advantages:

1. Instead of inducing a $[0, 2\pi]$ modulation working with a single heater, it allows to obtain a $[-\pi,+\pi]$ shift with lower power through the switch of the operating resistor.

2. It guarantees a back-up plan (using a $[0, 2\pi]$ single resistor) in the case one resistor is damaged.

In good agreement with the model in equation 5.1, a linear behaviour is obtained. The slope of the fitting of experimental data allows to retrieve the experimental a

74
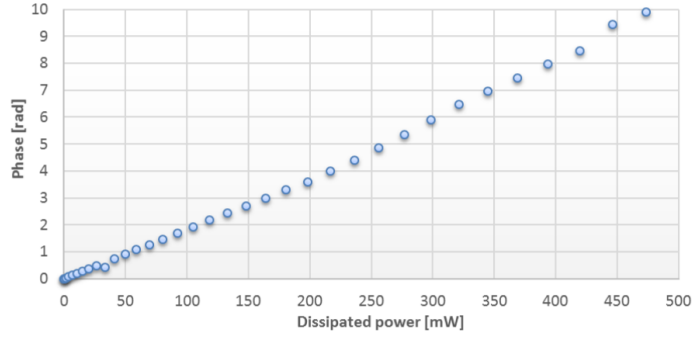
a)
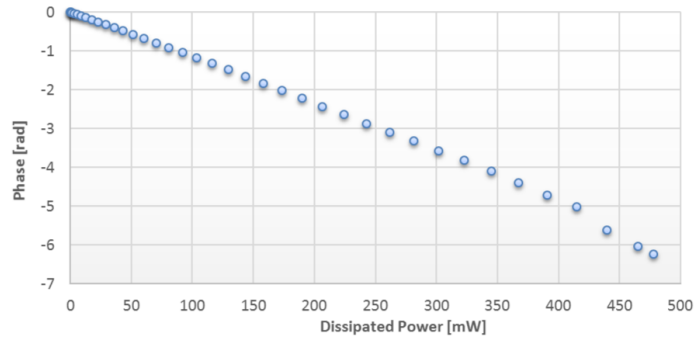
b)

Figure 5.1.4: Experimental characterization with classical light at 780 nm. The phase accumulated between the two arms of the directional coupler is plotted as a function of the dissipated power on the resistance R_C and R_B in (a) and (b), respectively.

coefficients, which are reported in table 5.1.3 . The difference in the a values of shared heaters can be attributed to a possible misalignment of resistors on the directional couplers' arms and the neglected effect of the transition regions between the pads and the wires.

Resistor parameter			
Resistor	Experimental resistance [Ω]	α [rad/W]	π Power [W]
A	116	12.3 - 15.6	0.25 - 0.2
B	111	12.5 - 18.3	0.25 - 0.17
C	98	20.5	0.15
F	98	13.5	0.23
G	128	12 - 14.5	0.26 - 0.22

Table 5.1.3: A schematic with the properties of the resistors is reported. The two values in the α and π Power columns are referred to the action of the thermal phase shifters on the corresponding devices: i.e. the first element refers to the phase modulation induced on the lower arm of the upper directional coupler, while the second is related to the upper arm of the lower directional coupler

5.2 DIRECTIONAL COUPLER AT TELECOM WAVELENGTH

FABRICATION PARAMETERS

Exploiting femtosecond laser writing technique, single mode waveguides at 1560 nm wavelength can be realized using the same fabrication setup (see Figure 3.1.1) just tailoring the processing parameters. The waveguides were machined in Corning EAGLE2000 borosilicate glass. The optimized fabrication parameters for single mode guiding at 1560 nm wavelength are summarized in Table 5.2.1. The structures were fabricated buried at 170 μm beneath the glass surface, since straight waveguides present the lowest propagation loss at this inscription depth. At the operation wavelength, the waveguides support a single gaussian mode of almost circular profile with 15.5 μm $1/e^2$ diameter. Coupling losses have been estimated to be 0.37 dB with respect to single mode fibers with mode dimension of 10.4 x 10.4 μm^2. Measured propagation losses are 0.3 dB/cm. The bending losses are in the order of 0.4 dB/cm for the 90 mm bending radius adopted.

Fabrication parameters		
Laser system	Yb:KYW cav. dump.	
Wavelength	1030 nm	
Repetition rate	1 MHz	
Pulse energy	370 nJ	
Translation speed	40 mm/s	
Objective	0.6 NA	

Table 5.2.1: Waveguide writing parameters used for building the balanced directional coupler at 1560 nm. Microscope image of the waveguide cross-section is also shown.

GEOMETRY

To define the geometry of a planar directional coupler we had to determine the waveguide separation at the input and output, the coupling distance d and the interaction length L.

The waveguide separation at the input and the output was determined by the coupling with the other devices and was set at 127 μm.

In the definition of the coupling distance d we had to take into account the following trade-off:

- Small coupling distance implies a bigger coupling coefficient k and therefore shorter interaction length L. As a consequence, more compact couplers can be fabricated.

- If the coupling distance is too small, the inscription process of the second waveguide could influence/damage the first waveguide already written and cause an increase in the insertion losses. This additional term in the inhomogeneity of the refractive index profile of the first waveguide could lead to an asymmetry in the propagation losses between the two arms and a different splitting ratio depending on the excited input of the directional coupler.

Being the last occurrence destructive for the output state, we decided not to push excessively towards the reduction of the coupler length. We performed a
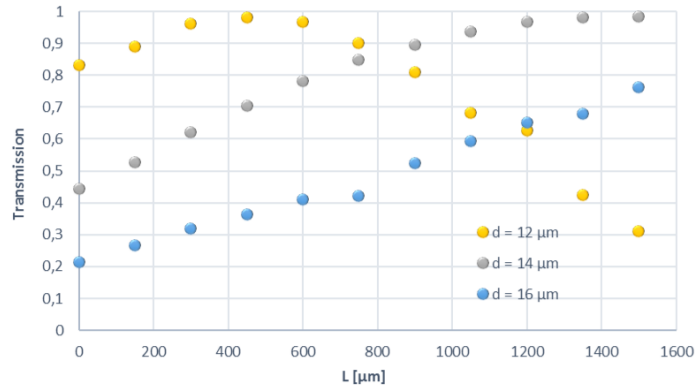
Figure 5.2.1: Experimental transmission of directional couplers fabricated with different interaction lengths, measured at 1550 nm wavelength for the polarization V. The behaviour of different coupling distance is reported. It is possible to observe that evanescent field coupling occurs even with null interacting length, due to the coupling originating already in the curved segments of the approaching waveguides.

transmission analysis on a set of three different coupling distances 12, 14, 16 μm by fabricating several directional couplers with different interaction length. The corresponding measurements are reported in Figure 5.2.1. The possibility of achieving a splitting ratio different from zero with no straight segment is caused by the coupling between modes in the two curved regions, where the waveguides are brought closer. The coupling distances d = 12 μm and d = 14 μm were discarded: they presented a splitting ratio above or near the 50 % at zero interaction length, therefore it would be possible not to obtain a balanced beam splitter with short L in a successive run due to fabrication tolerances.

Fixed the coupling distance d at 16 μm, several directional couplers have been fabricated varying the interaction length L, spanning the range 500 ÷ 1400 μm around the previously found $L_{50/50} \sim 900$ μm with a step of 50 μm.

78

Chosen BS device	
Coupling Distance	16 μm
Interaction Length	700 μm
Operating Wavelength	1560.4 μm
Splitting Ratio	50.2/49.8
Insertion Losses	2.72 dB
Mode Size	14.5 x 16.5 μm^2

Table 5.2.2: The design parameters and the performance of the selected directional coupler.

CHARACTERIZATION

Transmissivities and reflectivities of all the fabricated directional couplers were measured and the characteristics of the best device are reported in Table 5.2.2. It presents a transmissivity of 49.8 % at a wavelength of 1560 nm and insertion losses of 2.72 dB. A reduction of the losses could be achieved making the device more compact by lowering the length of the straight segments and therefore the propagation losses. A spectral characterization was also performed and reported in Figure 5.2.2. To perform this measurement, we used a tunable laser (Santec MLS-2000) with a wavelength range from 1450 to 1600 nm. The experimental splitting ratio of the directional coupler presents a linear behavior with respect to the input wavelength. The percentage variation of the splitting ratio, obtained from the fitting, can be estimated to 0.15 %/ nm.
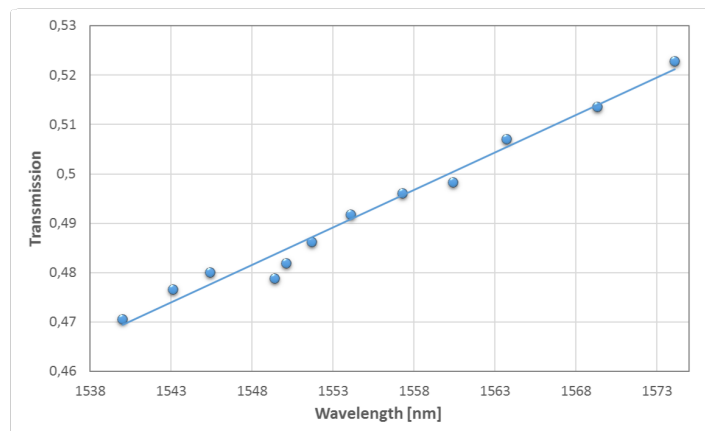
Figure 5.2.2: Experimental characterization of the splitting ratio of the directional coupler as a function of the input wavelength. The best fit is also reported.

6

Nonlinear phenomena in waveguides

This chapter deals with the development of an array of two waveguides in a non-linear medium through femtosecond laser micromachining. The requirements for this chip are as follows:

- Generation of twin-photons at telecom wavelength through spontaneous parametric down conversion.

- High generation yield: it implies the preservation of the nonlinear coefficient in the fabrication of waveguides.

- High indistinguishability between daughter photons generated from different waveguides.

- Good extraction yield: it implies acceptable losses at telecom wavelength.

In section 6.1 the selected substrate and a preliminary study on its properties are introduced. The choice of the fabrication technique is reported in section 6.2. Section 6.3 deals with the preliminary fabrication on the substrate and optimum processing parameters. In section 6.4 the results of the characterization of waveguides with classic light are presented.

6.1 MgO:LiNbO3

The substrate is a z-cut periodically-poled magnesium-doped lithium niobate (MgO:LiNbO3) supplied by Covesion (MSHG1550-1.0-20). Lithium niobate is one of the most employed material for nonlinear optics applications due to its high nonlinear optic coefficients (among the highest of all inorganic materials) and its transparency in the range from 350 to 5000 nm, which provides low loss for both the fundamental and second harmonic signals in visible light generation. The wide employment of this material leads to the development of a very stable manufacturing technology for the production of highly reproducible crystals. A drawback of LiNbO3 is its tendency to show photorefractive effects, which limit its high-power application and confines the operating temperature in the 100-200 °C range. In fact, in conditions of high optical intensity, electrons are released as free-carriers and redistributed around the irradiated region, hence causing a spatial variation of the refractive index, which can lead to a distortion of the output beam or even to a permanent damage of the crystal. The advantage of magnesium-oxide doping is an increase of damage threshold: the addition of 5 % MgO significantly increases the photorefractive and optical resistance of the crystal, while preserving its nonlinear coefficient. For that reason MgO:PPLN is more suitable for high-power applications and it can be operated at room temperature for second harmonic generation (SHG) with input telecom wavelength. The possibility to work at room temperature is a key advantage for our application, since it only requires temperature stabilization and not a temperature increase with a dedicated oven. Operating at 100 °C or above would have consequences not only on the laser-written waveguides in the nonlinear device (see section 6.2), but it would require to characterize

the linear integrated optical components at that temperature making the whole process labor intensive and time-consuming. It would introduce criticality also in the chip-chip alignment and in the fiber-chip coupling. The footprint of the nonlinear substrate is as follows: thickness of 1 mm, width of 10 mm and length of 20 mm. Despite longer crystal length implies an higher conversion efficiency in an ideal crystal due to their linear relation, the maximum useful crystal length is limited by several factors. A simple model, which takes only propagation losses in consideration, allows us to retrieve an approximated optimum length of the crystal. In figure 6.1.1 (a), the efficiency of the SHG process is plotted as a function of the crystal length in the case of PL $\sim$ 1 dB/cm for pump, signal and idler. In figure 6.1.1 (b) the optimum length as a function of PL is reported. As crystal length increases, the nonlinear conversion process becomes more sensitive to overall and local changes in temperature, strain and other factors affecting the difference in refractive indexes. Therefore asymmetry in the poling period and disuniformity in the fabricated waveguide impose an additional constrain in the effective length of the nonlinear crystal. After this preliminary pondering, we chose the device with a length of 20 mm. The MgO:PPLN contains five 1 mm - wide poling periods with $\Lambda = 19.2, 19.5, 19.8, 20.1, 20.4$ μm. Before proceeding with the purchase of the above substrate, a preliminary calculation of quasi- phase-matching curves were performed. Starting from the phase-matching equation:

$$k_{\mathrm{p}} = k_{\mathrm{s}} + k_{\mathrm{i}} + \frac{2\pi}{\Lambda} \qquad (6.1)$$

We rewrote it in terms of wavelength:

$$\frac{n_{\mathrm{p}}}{\lambda_{\mathrm{p}}} = \frac{n_{\mathrm{s}}}{\lambda_{\mathrm{s}}} + \frac{n_{\mathrm{i}}}{\lambda_{\mathrm{i}}} + \frac{1}{\Lambda}, \qquad (6.2)$$

where n_{p}, n_{s} and n_{i} are the temperature dependent refractive indexes for the pump, the signal and the idler, respectively. Energy conservation allows us to fur-
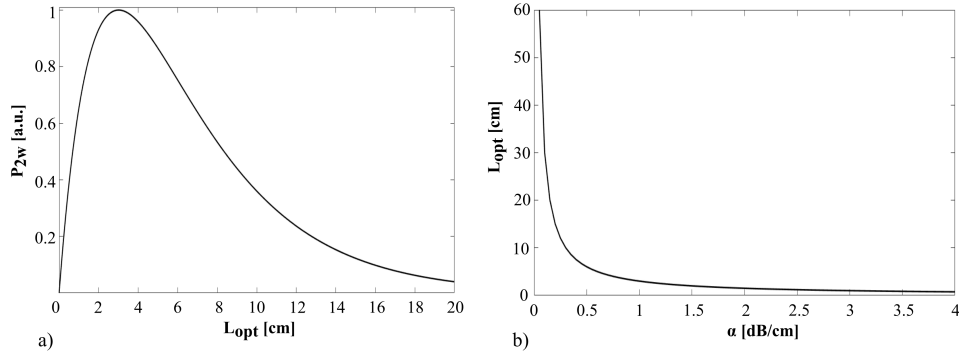
Figure 6.1.1: In figure (a) an estimation of SHG efficiency is represented as a function of the total length of the device setting the propagation losses to 1 dB/cm for pump, signal and idler. The curve presents a maximum value, which means that a longer device will not lead to an increase in the generation efficiency. In figure (b) the optimum length is plotted as a function of propagation losses of the device. As expected, the optimum length diverges in the case of an ideal crystal. The absolute value retrieved by the model must be taken with a grain of salt, since the related approximations are really rough.

ther simplify the simulation leading to the following equation:

$$\frac{n_p(T)}{\lambda_p} = \frac{n_s(T) - n_i(T)}{\lambda_s} + \frac{n_i}{\lambda_p} + \frac{1}{\Lambda(T)} \tag{6.3}$$

In addition to the temperature dependence of the refractive indexes, a small contribution is given by the thermal expansion of the crystal, that leads to a change of the poling period. It can be summarized by the following equation:

$$\Lambda(T) = \Lambda_o[1 + \alpha(T - T_o) + \beta(T - T_o)^2], \tag{6.4}$$

being $\alpha = 1.53 \cdot 10^{-5}\,\mathrm{K}^{-1}$, $\beta = 5.3 \cdot 10^{-9}\,\mathrm{K}^{-1}$ and $T_o = 19\,°C$.

The temperature dependent Sellmeier equations for 5 % MgO:LiNbO$_3$ can be found in [79]. Replacing all of the above term for Type-o SPDC (e → e + e), the phase-matching equation can be solved for a given period of poling and the results are reported in Figure 6.1.2. The wavelength of signal and idler for degenerate SPDC can be retrieved by the intersection between the black dash-dotted line and

the phase-matching curves. The dashed curves refer to momentum conservation at room temperature, while the solid ones represent QPM curves at 35 °C temperature. It is worth to underline that QPM gives the access to the highest tensor element d_{33} of the nonlinear susceptibility of the crystal. In fact, the second order nonlinear polarization of lithium niobate can be represented as follows:

$$
\begin{pmatrix} P_x \\ P_y \\ P_z \end{pmatrix} = 2 \cdot \begin{pmatrix} 0 & 0 & 0 & 0 & d_{31} & -d_{22} \\ -d_{22} & d_{22} & 0 & d_{31} & 0 & 0 \\ d_{31} & d_{31} & d_{33} & 0 & 0 & 0 \end{pmatrix} \begin{pmatrix} E_x^2 \\ E_y^2 \\ E_z^2 \\ 2E_z E_y \\ 2E_z E_x \\ 2E_x E_y \end{pmatrix} \tag{6.5}
$$

To achieve the highest conversion efficiency exploiting the d_{33} coefficient, which is equal to 25 pm/V, the polarization of all the interacting waves must be parallel to the z-axis of the crystal.

6.2 INSCRIPTION TECHNIQUE

As stated in paragraph 2.3.2, different fabrication configurations are available in crystals; each of them is characterized by the inscription geometry of the tracks. Before proceeding in the research of processing parameters, it was necessary to choose the proper configuration for our application. PPLN is a widely studied substrate and several articles on waveguide fabrication were published. The preservation of the nonlinear properties of the material and indistinguishability between waveguides realized in the same fabrication run are key requirements. First we introduce a figure of merit in the SHG process: the normalized conversion efficiency η^*, which is defined as:

$$
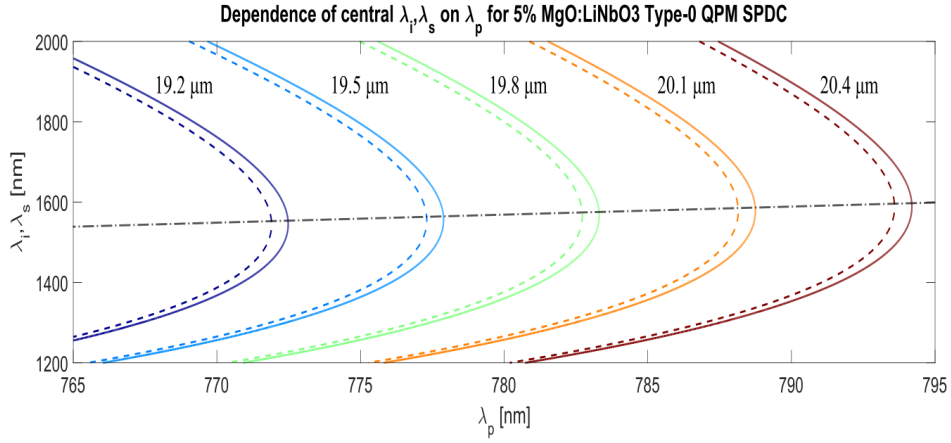\eta^* = \frac{P_{2w}}{(P_w L)^2}, \tag{6.6}
$$

Figure 6.1.2: Dependence of the signal and idler center wavelengths on the pump wavelength for 5 % MgO:LiNbO3 QPM SPDC twin-photon generation crystal. The intersections between QPM curves and the black dash-dotted line indicate degenerate points. Varying the temperature, a red-shift of the degenerate points can be observed: dashed and solid lines satisfy QPM condition for poling periods $\Lambda = 19.2, 19.5, 19.8, 20.1, 20.4$ μm at 25 and 35 °C, respectively.

where P_{2w} is the power of second harmonic, P_w is the power of the pump and L is the length of the device.

TYPE I: The guiding structure is directly inscribed by the femtosecond laser pulses and it generally suffers from the disruption of the nonlinear properties. Nevertheless, a distinctive multiscan approach [41] was exploited to minimize the effects on the nonlinear coefficient. Indeed, multiscan offers the possibility to keep the single scan energy to a level that minimizes the nonlinear interaction and to arbitrary control the cross-sectional shapes of the waveguide. The realization of single-mode waveguides both at fundamental and SHG wavelength was achieved leading to an efficient frequency doubling (SHG) at 1567 nm and a normalized conversion efficiency of 6.5 % W⁻¹ cm⁻². However, the guiding structure undergoes thermal annihilation above 200 °C, when point defects are washed out [66]. Thermal stability at room temperature of multiscan waveguides has been demon-

Waveguide configuration			
Type	λ_w [nm]	η^* [W^{-1} cm^{-2}]	PL [dB/cm]	Reference
I - Multiscan	1567	6.5	0.6	[41]
II	1064	2.5	1	[81]
III	1064	0.06	13.3	[80]

Table 6.2.1: A brief report on the results of different inscription technique by femtosecond laser writing in PPLN

strated, while the performances of single-scan waveguides deteriorate even in standard conditions.

TYPE II: In this configuration the nonlinear coefficient is intrinsically preserved, since the guiding structure is not directly affected by the laser pulses. In addition, type II structures present an high thermal resilience allowing their employment in high power applications, where an operating temperature above 200 °C is exploited to avoid photorefractive effects. Single mode guiding at both fundamental and second harmonic wavelength was achieved. Nevertheless, due to the small overlap between the guiding modes, the obtained normalized conversion efficiency was limited to 2.5 % W^{-1} cm^{-2}.

TYPE III: Second harmonic generation has been demonstrated in depressed cladding waveguide [80]. Nevertheless, the performance in term of losses and normalized conversion efficiency are not comparable with the above configurations. For the sake of completeness, it is worth mentioning that also the quasi phasematching periodic poling was realized by a direct laser-induced modulation of the nonlinearity inside the waveguide core.

Since working at high temperature is not a necessary condition and considering available experimental setup and performance, we decided to adopt the multiscan approach of type I waveguides.
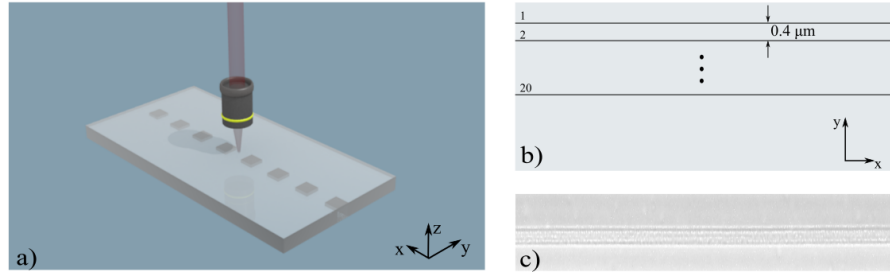
Figure 6.3.1: In figure (a) a schematic of the fabrication setup for waveguide inscription in z-cut MgO:PPLN is represented. The geometry of the adopted multiscan configuration is sketched in Figure (b) : 20 tracks are machined in the x direction, each scan is shifted by 0.4 μm from the other in the y direction. In Figure (c) a top-view microscope image of the waveguide in MgO:PPLN is reported.

6.3 FABRICATION PARAMETERS

Preliminary experiments were performed in the unpoled regions of the crystal with the experimental setup in Figure 3.1.1. The repetition rate of the laser pulses was locked to 1 MHz, while the laser linear polarization was set in the y direction. A 50X microscope objective (NA 0.6) was employed to focus the femtosecond laser pulses inside the substrate. A scan of the pulse energy, translation speed and inscription depth was carried out in order to find the combination of parameters, that leads to single-mode waveguides both at fundamental and second harmonic wavelengths. Each waveguide was fabricated by 20 scans in the x direction, spaced by 0.4 μm in the y direction. As indicated by [66], the femtosecond-laser-written waveguides support only the TM polarization. After this previous optimization, we started to fabricate waveguides in the poling periods, which do not have a periodicity useful for our application. In particular, as indicated by table 6.3.1, we focused our attention on the photons generated in the poled regions with poling periods Λ = 19.2 ; 19.5 and 19.8 μm, since their degenerate wavelengths are inside the C-band at room temperature. In the C-band the fibers, which will be used to

collect the emitted photons, present low losses and the efficiency of the employed single-photon detectors is higher. As a consequence, poling regions with Λ = 20.1; 20.4 μm were employed for preliminary fabrications and characterizations.

Waveguide configuration	
Λ [μm]	Degenerate Wavelength [nm]
19.2	1542
19.5	1553
19.8	1565
20.1	1577
20.4	1587

Table 6.3.1: The degenerate wavelength for SPDC process in MgO:PPLN at room temperature. A red-shift tuning of the emitted wavelength can be obtained increasing the operating temperature.

The optimum parameters are reported in Table 6.3.2.

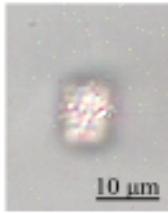| Fabrication parameters		
Laser system	Yb:KYW cav. dump.	
Wavelength	1030 nm	
Repetition rate	1 MHz	
Pulse energy	180 nJ	
Translation speed	50 mm/s	
Inscription depth	100 μm	10 μm
Objective	0.6 NA	

Table 6.3.2: Waveguide writing parameters used for waveguide inscription in 5% MgO:LiNbO3. Microscope image of the waveguide cross-section is also reported.

6.4 NONLINEAR ANALYSIS

6.4.1 INTRODUCTION

The nonlinear behaviour of the waveguides was tested via SHG process (see 3.2.5). The characterization of the periodically poled waveguides gave us the access to the following information:

- Correct wavelength for spectrally degenerate process. Since SHG is the Hermitian conjugate process of degenerate SPDC, the peak wavelength of SHG curve directly reports the wavelength combination to phase-match the degenerate SPDC process.

- Bandwidth of the SHG process: it allows us to compare the similarity in the nonlinear properties between different waveguides.

A numerical integration of the coupled-mode equations was performed to interpret the experimental results:

$$\frac{dA_w}{dz} = -i\,k^*\,A_w^*\,A_{2w}\,e^{-i\Delta k_{QPM}z} - \alpha_w\,A_w$$

$$\frac{dA_{2w}}{dz} = -i\,k\,A_w^2\,e^{i\Delta k_{QPM}z} - \alpha_{2w}\,A_w \tag{6.7}$$

$$k^2 = \frac{2\,w^2}{\varepsilon_0 c^3}\,\frac{d_{\textit{eff}}^2}{n_w^2\,n_{2w}\,S_{\textit{eff}}},$$

where A_i is the field amplitude of the fundamental or second harmonic; α_i is the propagation loss coefficient and z is the propagation coordinate. The refractive index n_i and the phase mismatch $\Delta k_{QPM} = k_{2w}$ - $2k_w$ - $2\pi/\Lambda$ were calculated through the temperature dependent Sellmeier equation. The $S_{\textit{eff}}$ is the effective waveguide cross-sections computed by the overlap integral of the mode transverse distributions, while the effective nonlinear coefficient for first order quasi-phase-matching is $d_{\text{eff}} = 2d_{33}/\pi$.

6.4.2 Preliminary measurements

A preliminary characterization of nonlinear properties was performed on waveguides fabricated in different runs. This measurement allowed us to retrieve an indication on our fabrication process in terms of preservation of the nonlinear coefficient and reproducibility. The results are presented in Figure 6.4.1 and in Table 6.4.1. The central peak wavelength of the inscribed waveguides drifts away from the one calculated by means of coupled equations. The model does not take into account the effective refractive index of guided mode in the quasi-phase-matching calculation. According to the different guided spatial modes, a modification of the effective indices $n_{eff,i}$ occurs leading to a translation of the phase-matching function in frequency space. Starting from the coupled equations, the shift $\Delta\lambda_o$ can be achieved in the following ways:

- An error of 0.85 % in the poling period from the one indicated by the supplier: $20.4 \ \mu m \ \rightarrow \ 20.58 \ \mu m$.

- $\Delta n \simeq 6 \cdot 10^{-3}$ induced by guiding effect at both fundamental and second harmonic wavelengths.

- A combination of the two terms above.

Since a measurement of $n_{eff,i}$ can not be easily performed and no information on the tolerances in the fabrication process of the poling period is reported on data-sheets, the weight of each term can not be retrieved. A slight deviation in the phase-matched wavelength between fabricated waveguides was also disclosed. It can be attributed to fabrication tolerances and to a not perfect stabilization of operating temperature. The bandwidths of the SHG process were estimated from the fitting curves and were compared to the bandwidth calculated from the theoretical curve in order to retrieve the effective interaction length L_{eff}. In fact, the parameter L_{eff} is directly related to the width of the main curve and the positions of the zeros. Since the experimental bandwidths were smaller than the theoretical one (1.518 nm), a value of $L_{eff} > L$ was retrieved : obviously this result has no physical
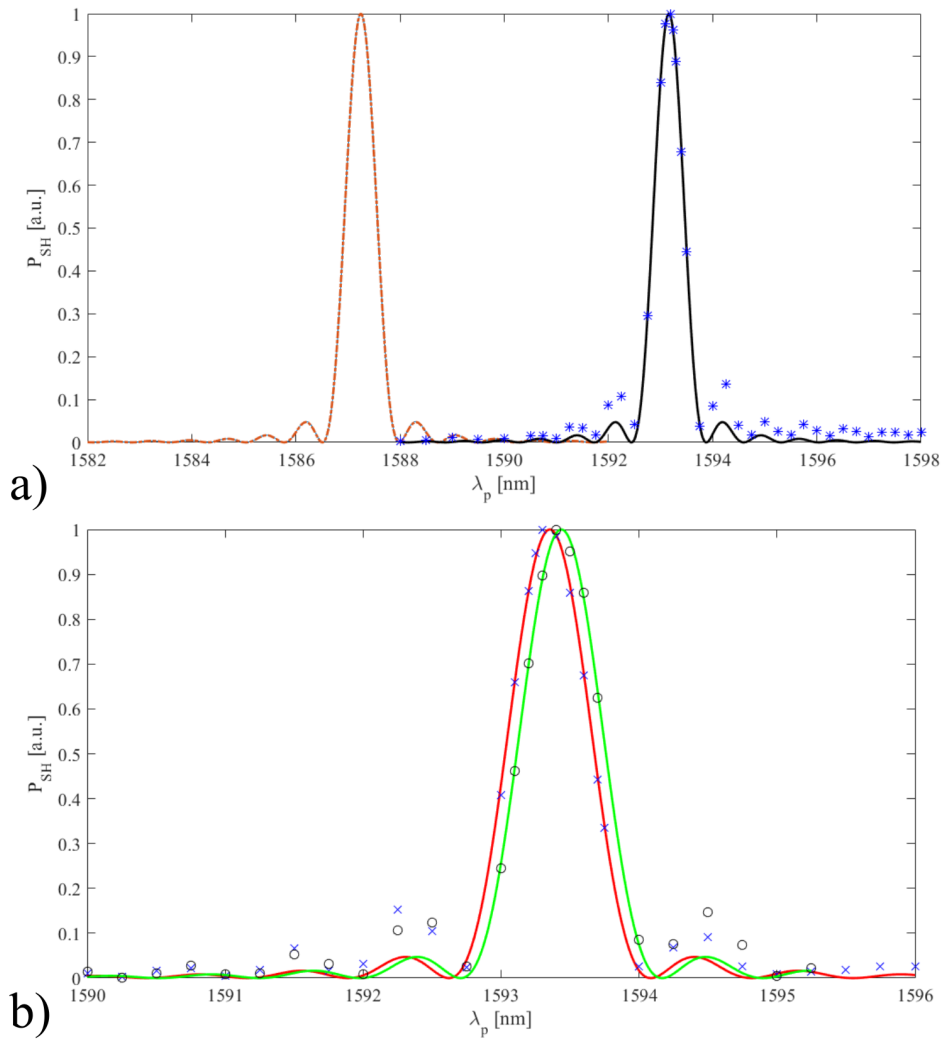
91

Figure 6.4.1: In Figure (a) the experimental points and the fitting curve, referred to waveguide 1 (see Table 6.4.1), are represented with the theoretical curve (dotted-dashed line) calculated from coupled equation. A shift of ~ 6 nm in the central phase-matched wavelength is evident from the plot. This deviation is ascribable to guiding effect on the propagation constants. In Figure (b) the SHG curves of waveguides 2 and 3, fabricated in the same run, are reported. The solid lines represent the fitting curve, while the circles and the crosses represent the experimental data. A difference of ~ 80 pm in the peak wavelength between the two waveguides can be retrieved from the fit.

92

Dummy SHG waveguides		
Waveguide	Central Wavelength [nm]	Bandwidth [nm]
1	1593.16	1.456
2	1593.36	1.464
3	1593.44	1.471

Table 6.4.1: A report of the performance of the dummy SHG waveguides: waveguide 1 was fabricated with the same parameters in a different run respect to waveguides 2 and 3. A difference in the peak wavelength between the fitted curves can be calculated. The bandwidth of the process is also reported.

meaning. Two factors has not been considered in the model: the guided modes effective index instead of the bulk index in the theoretical calculation, and the resolution of the experimental curves, i.e. only few measured points were taken on the main peak. Since it was a preliminary characterization, we decided not to carry out additional investigation and we concluded that the crystal length was more or less completely exploited in the generation process. The presence of higher shoulders next to the main peak with respect to the fit is an indication of slight disuniformity in the fabricated waveguides.

6.5 FINAL WAVEGUIDES

6.5.1 FABRICATION PARAMETERS

Due to the presence of a scratch at the output facet of the crystal in the proximity of the selected poling periods, a polishing was performed in order to permit the coupling of light. As a result of this procedure the anti-reflection coating, which allowed to reduce the reflectivity R below $1\,\%$ at $775/1550$ nm on both input/output facets, was removed. Another drawback was the reduction of the final length of the device to 1.83 cm. Since the crystal surface was not perfectly flat, the inscription depth was redefined in order to retrieve the previous focusing condition leading to slightly modified fabrication parameters as indicated by Table 6.5.1. A pair of sin-

gle mode waveguides (both at fundamental and at second harmonic wavelength) was machined in each selected poling period. The mode size was 12.5 x 12.1 μm^2 at 780 nm and 18.2 x 16 μm^2 at 1550 nm. In order to make the coupling with the linear devices possible, the input/output distance of the pair was set at 127 μm.

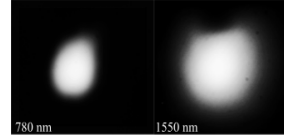| Fabrication parameters		
Laser system	Yb:KYW cav. dump.	
Wavelength	1030 nm	
Repetition rate	1 MHz	
Pulse energy	175 nJ	
Translation speed	50 mm/s	
Inscription depth	105 μm	
Objective	0.6 NA	

Table 6.5.1: Definite waveguide writing parameters used for waveguide inscription in 5% MgO:LiNbO3. Mode profile both at fundamental and second harmonic wavelengths.

6.5.2 SHG CHARACTERIZATION

The characterization of the nonlinear properties of the poled waveguides ($\Lambda = 19.5 \ \mu m$) was performed through the method described in 3.2.5. The automatized wavelength sweep and intensity acquisition were necessary due to the presence of fast fluctuations on the expected curve. In fact, after the polishing procedure and the consequent removal of the antireflection coating, the crystal behave like a Fabry-Perot interferometer, where the air/MgO:PPLN interfaces act as the end mirrors of the optical cavity. The acquired images were filtered by removing the spectral components of etalon and the fits of experimental data are reported in Figure 6.5.1 (c). As for the preliminary results (see 6.4.1), a shift in the phase-matched wavelength of about 6 nm with respect to the theoretical curve was observed. The bandwidth of the two curves are $\Delta\lambda_{wg1} \approx \Delta\lambda_{wg2} \approx 1.571$ nm. Comparing the theoretical bandwidth with the experimental one, the retrieved value for the effective length L_{eff} was about 1.76 cm, which can explain the higher shoulder aside from

SHG waveguides		
Waveguide	Central Wavelength [nm]	Bandwidth [nm]
1	1560.62	1.571
2	1560.64	1.571
Theoretical	1554.68	1.509

Table 6.5.2: A report of the performance of the final SHG waveguides: the bandwidth and the central wavelength of fabricated waveguides are reported.

the next peak. The phase matched wavelengths of the two waveguides are slightly different, nevertheless the overlap O between the two curves is above 0.99 % : the nonlinear properties of the two waveguides are practically the same. The SPDC degenerate process will be phase-matched at λ_p = 780.31 ±0.01 nm →1560.62 ±0.02 nm at room temperature.

6.5.2.1 ETALON

An evaluation of propagation losses of the integrated waveguides at telecom wavelength can be performed employing the Fabry-Perot resonance technique. The wavelength separation between two adjacent peaks in the transmission profile is the so called free spectral range (FSR) of the Fabry-Perot interferometer and is given by the following equation:

$$\Delta\lambda_{FSR} = \frac{\lambda^2}{2nd},$$
(6.8)

where λ is the working wavelength, n is the refractive index of the medium and d is the separation between the mirrors. Replacing λ = 1560 nm, d=1.83 cm and n the extraordinary refractive index of MgO:PPLN at λ, the theoretical FSR results as 31.1 pm. The comparison between the theoretical and the experimental (30.6 pm) values allows us to conclude that the transmission fluctuations are related to the fundamental wavelength. The figure of merit of the Fabry-Perot interferometer that is most sensitive to losses is the finesse. The finesse represents the number of beams interfering within the cavity to form the standing wave and can be defined as

the ratio between the free spectral range and the minimum resolvable bandwidth:

$$F = \frac{\Delta\lambda_{FSR}}{\Delta\lambda_{FWHM}} \tag{6.9}$$

The mean FWHM of a large number of peaks was computed leading to an experimental Finesse of 2.194. The relation between the finesse and the attenuation of light propagating inside the waveguide can be expressed as follows:

$$a\,L = \ln\left(R\frac{\cos\left(\pi/F\right)}{1 - \sin\left(\pi/F\right)}\right), \tag{6.10}$$

where a L is the attenuation of the device and R is the reflectivity of the mirrors. In the case of well polished waveguide end-facets perpendicular to the waveguide axis, the reflectivity will be equal to the Fresnel reflection coefficient:

$$R = \frac{(n - n_2)^2}{(n + n_2)^2}, \tag{6.11}$$

being n the refractive index of air and n_2 the refractive index of crystal. The refractive index of MgO:PPLN was calculated through Sellmeier equation at the operating wavelength and temperature, resulting in a reflectivity R $\sim$ 13 %.

Replacing all the experimental values in equation 6.10, we retrieve propagation losses $\sim$ 1.48 dB/cm for both waveguides. This result can be compared to the previous losses analysis based on the method reported in section 3.2.4: IL $\sim$ 4.9 dB, FL $\sim$ 1.21 dB at both interfaces , CL $\sim$ 0.9 dB with a single mode fiber with mode size of 10.4x10.4 μm^2 and thus PL $\sim$ 1.51 dB/cm.
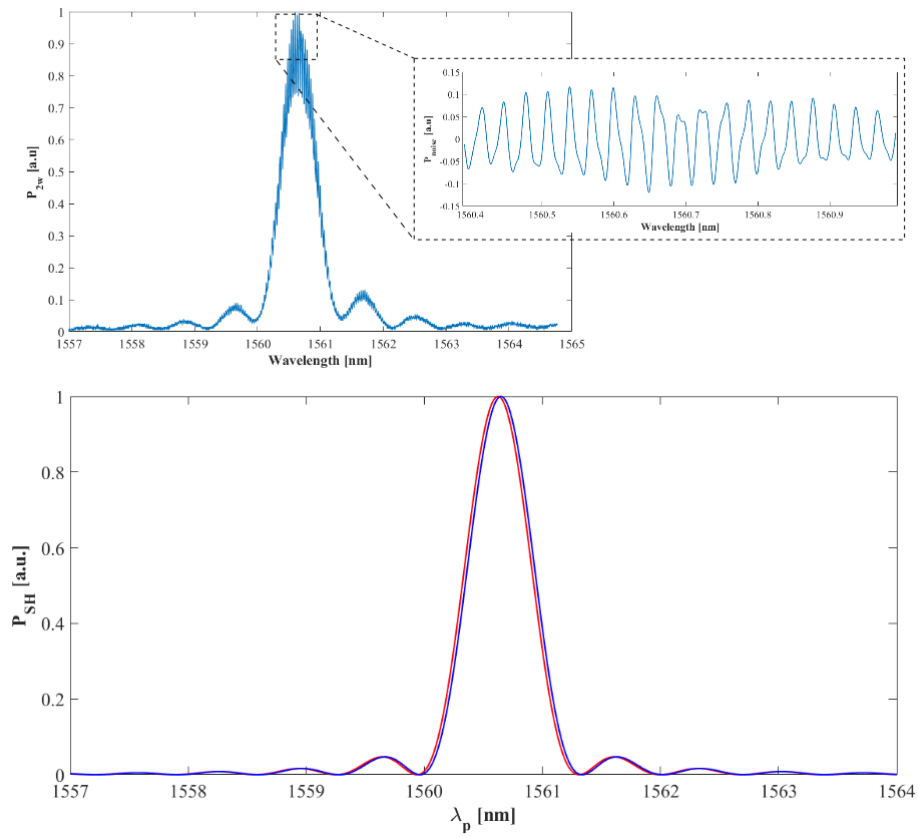
Figure 6.5.1: The SHG curve acquired with method 3.2.5 is reported. In the inset a part of the transmission fluctuation profile is sketched. The best fitting of the filtered experimental data in figure (a) are represented.

Conclusions

Integrated optical components for on-chip twin-photons source based on Spontaneous Parametric Down Conversion have been reported. The source exploits an hybrid approach being composed of three-cascaded chips in different substrates.

A balanced directional coupler at 780 nm wavelength was realized in aluminum-borosilicate glass through femtosecond laser micromachining. Gold thermal heaters were fabricated on the output arms of the directional coupler, allowing the low-power full control of the phase accumulated at the output ports of the first device.

A pair of parallel straight waveguides has been realized in periodically-poled magnesium-doped lithium niobate (MgO:PPLN), showing single mode behaviour at both fundamental and down-converted wavelength. A classical characterization through second harmonic generation (SHG) process has been performed in order to investigate the nonlinear properties of femtosecond laser written waveguides in terms of indistinguishability and generation efficiency (preservation of nonlinear coefficient and losses). An overlap above 99 % between the SHG curves obtained in two different waveguides has been reported. Comparable propagation losses of 1.48 dB/cm at telecom wavelength has been numerically calculated from experimental Finesse attenuation in the Fabry-Perot interferometer composed by MgO:PPLN/air interfaces.

In addition, a femtosecond laser written directional coupler at 1560 nm has been fabricated. The splitting ratio is 50 ± 1 % for a 10 nm range around the central wavelength of degenerate SPDC, allowing to preserve the state even with slight variations of the operating temperature.

The next step will be the alignment and coupling of the three components in order to characterize the quantum properties of the source. Future development would be to fabricate a polarization insensitive balanced directional coupler with an integrated half waveplate at 45° on its input arm, leading to the generation of a polarization-entangled state. The waveplate can be fabricated according to the method proposed by Corrielli et al. [82], where the tilting of the inscribed laser beam induces a tilt of the optical axis of the straight waveguides.

Ringraziamenti

Siamo giunti alla fine...

Vorrei ringraziare il Dr. Roberto Osellame per l'opportunità di lavorare nel suo fantastico gruppo di ricerca. Un grazie a tutti i suoi componenti per il tempo trascorso insieme tra esperimenti, pranzi ed il "Traditional Tea". Un grazie speciale ad Andrea per avermi insegnato a muovere i primi passi in un laboratorio di ottica e l'arte della fabbricazione di guide. Un enorme grazie a Giacomo per avermi consigliato e sopportato (la o al posto della u non è un refuso) in questi mesi. Un grazie particolare a Farid e Davide per il reciproco sostegno e le risate in laboratorio.

Vorrei ringraziare il Prof. Marco Marangoni per avermi ospitato nel suo laboratorio di Lecco. Un grande grazie a Davide ed a Riccardo per l'accoglienza e la disponibilità riservatemi.

Un grazie agli amici del Poli per averlo reso un posto speciale. Menzione d'onore per Alice e Ruggero: con voi i ritardi di Trenord sono sembrati quasi piacevoli.

Agli amici bandisti ed, in particolare ai trombettisti ("i migliori"), un ringraziamento speciale per le serate in allegria e quasi sempre accompagnate da buona musica (Perchè quasi? Chiedetelo a "i migliori", che a volte si dimenticano di suonare, ma non di chiacchierare XD).

Agli amici di sempre un grandissimo grazie!

Ultimo, ma non meno importante l'enorme ringraziamento a tutti i familiari che mi hanno sempre sostenuto con affetto ed incoraggiato.

Ai miei genitori vorrei dire solo grazie: qualsiasi aggettivo sminuirebbe il loro ruolo in questo percorso.

Bibliography

[1] M. Planck. Zur theorie des gesetzes der energieverteilung im normalspectrum. *Verhandl. Dtsc. Phys. Ges.*, 2:237, 1900.

[2] A. Einstein. Uber einen die erzeugung und verwandlung des lichtes betreffenden heurischen gesichtpunkt. *Annalen der Physik*, 17:132–148, 1905.

[3] Gilbert N Lewis. The conservation of photons. *Nature*, 118:874–875, 1926.

[4] R. H. Brown and R. Q. Twiss. Correlation between photons in two coherent beams of light. *Nature*, 177(4497):27–29, 1956.

[5] DF Walls and Gerard J Milburn. *Introduction in Quantum Optics*. Springer, 1994.

[6] R. J. Glauber. The quantum theory of optical coherence. *Physical Review*, 130(6):2529, 1963.

[7] B. Lounis and M. Orrit. Single-photon sources. *Reports on Progress in Physics*, 68(5):1129, 2005.

[8] M. Hijlkema, B. Weber, H. P. Specht, S. C. Webster, A. Kuhn, and G. Rempe. A single-photon server with just one atom. *Nature Physics*, 3(4):253–255, 2007.

[9] U Gaubatz, P Rudecki, M Becker, S Schiemann, M Külz, and K Bergmann. Population switching between vibrational levels in molecular beams. *Chemical physics letters*, 149(5-6):463–468, 1988.

[10] Z. Yuan, B. E. Kardynal, R. M. Stevenson, A. J. Shields, C. J. Lobo, K. Cooper, N. S. Beattie, D. A. Ritchie, and M. Pepper. Electrically driven single-photon source. *Science*, 295(5552):102–105, 2002.

[11] A Kiraz, M Ehrl, Th Hellerer, ÖE Müstecaplıoğlu, C Bräuchle, and A Zumbusch. Indistinguishable photons from a single molecule. *Physical review letters*, 94(22):223602, 2005.

[12] R. Brouri, A. Beveratos, J. Poizat, and P. Grangier. Photon antibunching in the fluorescence of individual color centers in diamond. *Optics letters*, 25 (17):1294–1296, 2000.

[13] E Wu, JR Rabeau, Gérard Roger, François Treussart, Heping Zeng, Philippe Grangier, Steven Prawer, and Jean-François Roch. Room temperature triggered single-photon source in the near infrared. *New Journal of Physics*, 9 (12):434, 2007.

[14] Andrew J Shields. Semiconductor quantum light sources. *Nature photonics*, 1(4):215–223, 2007.

[15] Edward Mills Purcell. Spontaneous emission probabilities at radio frequencies. *Physical Review*, 69:681, 1946.

[16] A. Muller, W. Fang, J. Lawall, and G. S. Solomon. Creating polarization-entangled photon pairs from a semiconductor quantum dot using the optical stark effect. *Physical review letters*, 103(21):217402, 2009.

[17] G Brida, IP Degiovanni, Marco Genovese, A Migdall, F Piacentini, SV Polyakov, and I Ruo Berchera. Experimental realization of a low-noise heralded single-photon source. *Optics express*, 19(2):1484–1492, 2011.

[18] D.C. Burnham and D.L. Weinberg. Observation of simultaneity in parametric production of optical photon pairs. *Physical Review Letters*, 25(2):84, 1970.

[19] P. G. Kwiat, K. Mattle, H. Weinfurter, A. Zeilinger, A. V Sergienko, and Y. Shih. New high-intensity source of polarization-entangled photon pairs. *Physical Review Letters*, 75(24):4337, 1995.

[20] J. Chen, A. J. Pearlman, A. Ling, J. Fan, and A.L. Migdall. A versatile waveguide source of photon pairs for chip-scale quantum information processing. *Optics express*, 17(8):6727–6740, 2009.

[21] JA Armstrong, N Bloembergen, J Ducuing, and PS Pershan. Interactions between light waves in a nonlinear dielectric. *Physical Review*, 127(6):1918, 1962.

[22] D. S. Hum and M. M. Fejer. Quasi-phasematching. *Comptes Rendus Physique*, 8(2):180–198, 2007.

[23] S. Tanzilli, H. De Riedmatten, H. Tittel, H. Zbinden, P. Baldi, M. De Micheli, D.B. Ostrowsky, and N. Gisin. Highly efficient photon-pair source using periodically poled lithium niobate waveguide. *Electronics Letters*, 37(1):26–28, 2001.

[24] J. Fan, A. Migdall, and LJ Wang. Efficient generation of correlated photon pairs in a microstructure fiber. *Optics letters*, 30(24):3368–3370, 2005.

[25] C. Söller, B. Brecht, P. J. Mosley, L. Y. Zang, A. Podlipensky, N. Y. Joly, P. St. J. Russell, and C. Silberhorn. Bridging visible and telecom wavelengths with a single-mode broadband photon pair source. *Physical Review A*, 81(3): 031801, 2010.

[26] B. J. Smith, P. Mahou, O. Cohen, JS Lundeen, and IA Walmsley. Photon pair generation in birefringent optical fibers. *Optics express*, 17(26):23589–23602, 2009.

[27] J. E Sharping, K. F. Lee, M. A Foster, A. C. Turner, B. S. Schmidt, M. Lipson, A. L. Gaeta, and P. Kumar. Generation of correlated photons in nanoscale silicon waveguides. *Optics express*, 14(25):12388–12393, 2006.

[28] H. Takesue and K. Inoue. 1.5-μm band quantum-correlated photon pair generation in dispersion-shifted fiber: suppression of noise photons by cooling fiber. *Optics express*, 13(20):7832–7839, 2005.

[29] Y. Huang and P. Kumar. Distilling quantum entanglement via mode-matched filtering. *Physical Review A*, 84(3):032315, 2011.

[30] J. L. O'Brien. Optical quantum computing. *Science*, 318(5856):1567–1570, 2007.

[31] E. Knill, R. Laflamme, and G. J. Milburn. A scheme for efficient quantum computation with linear optics. *Nature*, 409(6816):46–52, 2001.

[32] M. Varnava, D. E. Browne, and T. Rudolph. How good must single photon sources and detectors be for efficient linear optical quantum computation? *Physical review letters*, 100(6):060502, 2008.

[33] Hitoshi Inamori, Norbert Lütkenhaus, and Dominic Mayers. Unconditional security of practical quantum key distribution. *The European Physical Journal D*, 41(3):599–627, 2007.

[34] C. H. Bennett. Quantum cryptography: Public key distribution and coin tossing. In *International Conference on Computer System and Signal Processing, IEEE, 1984*, pages 175–179, 1984.

[35] Xiongfeng Ma, Bing Qi, Yi Zhao, and Hoi-Kwong Lo. Practical decoy state for quantum key distribution. *Physical Review A*, 72(1):012326, 2005.

[36] Nicolas Gisin, Grégoire Ribordy, Wolfgang Tittel, and Hugo Zbinden. Quantum cryptography. *Reviews of modern physics*, 74(1):145, 2002.

[37] Christoph Simon, Hugues De Riedmatten, Mikael Afzelius, Nicolas Sangouard, Hugo Zbinden, and Nicolas Gisin. Quantum repeaters with photon pair sources and multimode memories. *Physical review letters*, 98(19): 190503, 2007.

[38] A. N. Boto, P. Kok, D. S. Abrams, S. L. Braunstein, C. P. Williams, and J. P. Dowling. Quantum interferometric optical lithography: exploiting entanglement to beat the diffraction limit. *Physical Review Letters*, 85(13):2733, 2000.

[39] V. Giovannetti, S. Lloyd, and L. Maccone. Quantum metrology. *Physical review letters*, 96(1):010401, 2006.

[40] K.M.Davis, K.Miura, N.Sugimoto, and K.Hirao. Writing waveguides in glass with a femtosecond laser. *Optics letters*, 21(21):1729–1731, 1996.

[41] Osellame Roberto, Cerullo Giulio, and Ramponi Roberta. *Femtosecond Laser Micromachining, Photonic and Microfluidic Devices in Transparent Material.* Springer, 2012.

[42] L.V. Keldysh. Ionization in the field of a strong electromagnetic wave. *Soviet Physics JETP*, 20(5), 1965.

[43] R. Bruckne. Properties and structure of vitreous silica. i. journal of non-crystalline solids. *Journal of Non-Crystalline Solids*, 5(2):123–175, 1970.

[44] P. Dekker, M. Ams, G. D. Marshall, D. J. Little, and M. J. Withford. Annealing dynamics of waveguide bragg gratings: evidence of femtosecond laser induced colour centres. *Optics Express*, 18(4):3274–3283, 2010.

[45] S. Kanehira, K. Miura, and K. Hirao. Ion exchange in glass using femtosecond laser irradiation. *Applied Physics Letters*, 93(2):023112, 2008.

[46] J. W. Chan, T. Huser, S. Risbud, and D. M. Krol. Structural changes in fused silica after exposure to focused femtosecond laser pulses. *Optics Letters*, 26 (21):1726–1728, 2001.

[47] M. Sakakura, M. Shimizu, Y. Shimotsuma, K. Miura, and K. Hirao. Temperature distribution and modification mechanism inside glass with heat accumulation during 250 kHz irradiation of femtosecond laser pulses. *Applied Physics Letters*, 93(23):231112, 2008.

[48] L. Sudrie, M. Franco, B. Prade, and A. Mysyrowicz. Writing of permanent birefringent microlayers in bulk fused silica with femtosecond laser pulses. *Optics Communications*, 171(4):279–284, 1999.

[49] S. Juodkazis, K. Nishimura, S. Tanaka, H. Misawa, E. G. Gamaly, B. Luther-Davies, L. Hallo, P. Nicolaï, and V. T. Tikhonchuk. Laser-induced microexplosion confined in the bulk of a sapphire crystal: evidence of multimegabar pressures. *Physical review letters*, 96(16):166101, 2006.

[50] V. Ta'Eed, J. Baker, L. Fu, K. Finsterbusch, M. R. E. Lamont, D. J. Moss, Hong C. N., Benjamin J. E., D. Choi, S. Madden, and et al. Ultrafast all-optical chalcogenide glass photonic circuits. *Optics Express*, 15(15):9205–9221, 2007.

[51] J. Siegel, M. Fernàndez-Navarro, A. Garcia-Navarro, V. Diez-Blanco, O. Sanz, J. Solis, F Vega, and J. Armengol. Waveguide structures in heavy metal oxide glass written with femtosecond laser pulses above the critical self-focusing threshold. *Applied Physics Letters*, 86(12):121109, 2005.

[52] S. Sowa, W. Watanabe, T. Tamaki, J. Nishii, and K. Itoh. Symmetric waveguides in poly(methyl methacrylate) fabricated by femtosecond laser pulses. *Optics Express*, 14:291–297, 2005.

[53] R. R. Gattass and E. Mazur. Femtosecond laser micromachining in transparent materials. *Nature photonics*, 2(4):219–225, 2008.

[54] S. M. Eaton. *Contrasts in thermal diffusion and heat accumulation effects in the fabrication of waveguides in glasses using variable repetition rate femtosecond laser.* PHD Thesis, University of Toronto, 2008.

[55] G. Cerullo, R. Osellame, S. Taccheo, M. Marangoni, D. Polli, R. Ramponi, and S. De Silvestri P. Laporta. Femtosecond micromachining of symmetric waveguides at 1.5 μm by astigmatic beam focusing. *Optics letters*, 27(21): 1938–1940, 2002.

[56] R. Osellame, S. Taccheo, M. Marangoni, R. Ramponi, P. Laporta, D. Polli, S. De Silvestri, and G. Cerullo. Femtosecond writing of active optical waveguides with astigmatically shaped beams. *Journal of the Optical Society of America B*, 20(7):1559–1567, 2003.

[57] Y. Cheng, K. Sugioka, K. Midorikawa, M. Masuda, K. Toyoda, M. Kawachi, and K. Shihoyama. Control of the cross-sectional shape of a hollow microchannel embedded in photostructurable glass by use of a femtosecond laser. *Optics letters*, 28(1):55–57, 2003.

[58] M. Ams, G.D. Marshall, D.J. Spence, and M.J. Withford. Slit beam shaping method for femtosecond laser direct-write fabrication of symmetric waveguides in bulk glasses. *Optics Express*, 13(15):5676–5681, 2005.

[59] R.R. Thomson, A.S. Bockelt, E. Ramsay, S. Beecher, A.H. Greenaway, A.K. Kar, and D.T. Reid. Shaping ultrafast laser inscribed optical waveguides using a deformable mirror. *Optics Express*, 16(17):12786–12793, 2008.

[60] F. He, H. Xu, Y. Cheng, J. Ni, H. Xiong, Z. Xu, K. Sugioka, and K. Midorikawa. Fabrication of microfluidic channels with a circular cross section using spatiotemporally focused femtosecond laser pulses. *Optics Lettes*, 35 (7):1106–1108, 2010.

[61] R. Osellame, M. Lobino, N. Chiodo, M. Marangoni, G. Cerullo, R. Ramponi, R.R. Thomson H.T. Bookey, N.D. Psaila, and A.K. Kar. Femtosecond laser writing of waveguides in periodically poled lithium niobate preserving the nonlinear coefficient. *Applied Physics Letters*, 90(24):241107, 2007.

[62] N.D. Psaila, R.R. Thomson, H.T. Bookey, N. Chiodo, S. Shen, R. Osellame, G. Cerullo, A. Jha, and A.K. Kar. Er:Yb-doped oxyfluoride silicate glass waveguide laser fabricated using ultrafast laser inscription. *IEEE Photon. Technol. Lett.*, 20(2):126–128, 2008.

[63] L. Shah, A. Arai, S. Eaton, and P. Herman. Waveguide writing in fused silica with a femtosecond fiber laser at 522 nm and 1 MHz repetition rate. *Optics Express*, 13(6):1999–2006, 2005.

[64] W. Yang, P.G. Kazansky, Y. Shimotsuma, M. Sakakura, K. Miura, and K. Hirao. Ultrashort-pulse laser calligraphy. *Applied Physics Letters*, 93(17): 171109, 2008.

[65] D. J Little, M. Ams, P. Dekker, G. D. Marshall, J. M. Dawes, and M. J. Withford. Femtosecond laser modification of fused silica: the effect of writing polarization on Si-O ring structure. *Optics express*, 16(24):20029–20037, 2008.

[66] J. Burghoff, S. Nolte, and A. Tünnermann. Origins of waveguiding in femtosecond laser-structured LiNbO3. *Applied Physics A*, 89(1):127–132, 2007.

[67] F. Chen and J. R. Vàzquez de Aldana. Optical waveguides in crystalline materials produced by femtosecond laser micromachining. *Laser Photonics Rev.*, 8(2):251–275, 2014.

[68] L. Gui, B. Xu, and T. C. Chong. Microstructure in lithium niobate by use of focused femtosecond laser pulses. *IEEE Photonics Technology Letters*, 16(5): 1337–1339, 2004.

[69] J. Burghoff, C. Grebing, S. Nolte, and A. Tünnermann. Efficient frequency doubling in femtosecond laserwritten waveguides in lithium niobate. *Applied Physics Letters*, 89(8):081108, 2006.

[70] J. R. Macdonald, R. R. Thomson, S. J. Beecher, N. D.Psaila, H. T. Bookey, and A. K. Kar. Ultrafast laser inscription of near-infrared waveguides in polycrystalline ZnSe. *Optics Letters*, 35(23):4036–4038, 2010.

[71] A. Ròdenas and A. Kar. High-contrast step-index waveguides in borate nonlinear laser crystals by 3d laser writing. *Optics Express*, 19(18):17820–17833, 2011.

[72] A. Ródenas, G.A. Torchia, G. Lifante, E. Cantelar, J. Lamela, F. Jaque, L. Roso, and D. Jaque. Refractive index change mechanisms in femtosecond laser written ceramic nd: Yag waveguides: micro-spectroscopy experiments and beam propagation calculations. *Applied Physics B*, 95(1):85–96, 2009.

[73] A.G. Okhrimchuk, A.V. Shestakov, I. Khrushchev, and J. Mitchell. Depressed cladding, buried waveguide laser formed in a YAG: Nd 3+ crystal by femtosecond laser writing. *Optics letters*, 30(17):2248–2250, 2005.

[74] Y. Jia, N. Dong, F. Chen, J.R. V. de Aldana, S. Akhmadaliev, and S. Zhou. Ridge waveguide lasers in Nd: GGG crystals produced by swift carbon ion irradiation and femtosecond laser ablation. *Optics express*, 20(9):9763–9768, 2012.

[75] G. Corrielli. *Integrated photonic circuits by femtosecond laser writing for qubit manipulation, quantum cryptography and quantum-optical analogies*. PHD Thesis, Politecnico di Milano, 2015.

[76] A. Killi, A. Steinmann, J. Dorring, U. Morgner, M.J. Lederer, D. Kopf, and C. Fallnich. High-peak-power pulses from a cavity-dumped Yb:KY(WO4)2 oscillator. *Optics Letters*, 30(1891), 2005.

[77] A. Killi and U. Morgner. Solitary pulse shaping dynamics in cavity-dumped laser oscillators. *Optics Express*, 12:3397–3407, 2004.

[78] F. Flamini, L. Magrini, A. S. Rab, N. Spagnolo, V. D'ambrosio, P. Mataloni, F. Sciarrino, T. Zandrini, A. Crespi, R. Ramponi, et al. Thermally reconfigurable quantum photonic circuits at telecom wavelength by femtosecond laser micromachining. *Light: Science and Applications*, 4(11):e354, 2015.

[79] O Gayer, Z Sacks, E Galun, and A Arie. Temperature and wavelength dependent refractive index equations for mgo-doped congruent and stoichiometric linbo3. *Applied Physics B*, 91(2):343–348, 2008.

[80] Sebastian Kroesen, Kemal Tekce, Jörg Imbrock, and Cornelia Denz. Monolithic fabrication of quasi phase-matched waveguides by femtosecond laser structuring the $\chi(2)$ nonlinearity. *Applied Physics Letters*, 107(10):101109, 2015.

[81] Jens Thomas, Matthias Heinrich, Jonas Burghoff, Stefan Nolte, Antonio Ancona, and Andreas Tünnermann. Femtosecond laser-written quasi-phase-matched waveguides in lithium niobate. *Applied Physics Letters*, 91(15): 151108, 2007.

[82] Giacomo Corrielli, Andrea Crespi, Riccardo Geremia, Roberta Ramponi, Linda Sansoni, Andrea Santinelli, Paolo Mataloni, Fabio Sciarrino, and Roberto Osellame. Rotated waveplates in integrated waveguide optics. *Nature communications*, 5, 2014.